Titre: Title:	Flutter Instability of a Reconfiguring Beam with Large Displacement
Auteur: Author:	Mohammad Tari
Date:	2020
Type:	Mémoire ou thèse / Dissertation or Thesis
Référence: Citation:	Tari, M. (2020). Flutter Instability of a Reconfiguring Beam with Large Displacement [Mémoire de maîtrise, Polytechnique Montréal]. PolyPublie. https://publications.polymtl.ca/5256/

Document en libre accès dans PolyPublie
Open Access document in PolyPublie

URL de PolyPublie: PolyPublie URL:	https://publications.polymtl.ca/5256/
Directeurs de recherche: Advisors:	Éric Laurendeau, & Frederick Gosselin
Programme: Program:	Génie mécanique

POLYTECHNIQUE MONTRÉAL

affiliée à l'Université de Montréal

Flutter Instability of a Reconfiguring Beam with Large Displacement

MOHAMMAD TARI

Département de génie mécanique

Mémoire présenté en vue de l'obtention du diplôme de *Maîtrise ès sciences appliquées*

Génie mécanique

Avril 2020

Ce mémoire intitulé :

Flutter Instability of a Reconfiguring Beam with Large Displacement

présenté par **Mohammad TARI**
en vue de l'obtention du diplôme de *Maîtrise ès sciences appliquées*
a été dûment accepté par le jury d'examen constitué de :

Aouni LAKIS, président

Éric LAURENDEAU, membre et directeur de recherche

Frédérick GOSSELIN, membre et codirecteur de recherche

Mojtaba KHEIRI, membre

ACKNOWLEDGMENT

RÉSUMÉ

Les arbres et les plantes tirent bénéfice de leur flexibilité en réduisant la charge aérodynamique à laquelle ils sont confrontés en se pliant et en se déformant. La flexibilité est donc un avantage, permettant une reconfiguration et une réduction de la traînée. Cependant, il est bien connu que la flexibilité est également à l'origine de nombreux phénomènes de vibration induite par l'écoulement tels que le flottement, qui peuvent être associés à des contraintes dynamiques élevées. Le but de cette recherche est de savoir si le flottement limite les avantages de la reconfiguration. Dans ce but, nous considérons la reconfiguration d'une plaque plane sous écoulement d'air pour imiter la reconfiguration complexe de vraies plantes. En particulier, nous examinons la dynamique d'une plaque plane initialement positionnée perpendiculaire à l'écoulement du fluide et fixée à sa ligne médiane. Dans la partie numérique, nous développons un solveur structural considérant les grands déplacements en supposant qu'un modèle de poutre d'Euler-Bernoulli représente le mouvement des plaques en deux dimensions. Nous utilisons un code CFD pour la simulation du champ d'écoulement. Nous utilisons une technique itérative partitionnée pour coupler les solveurs structural et fluide afin d'assurer la convergence des variables de structure et d'écoulement au niveau de l'interface. De plus, nous étudions les caractéristiques de flottement d'une poutre en reconfiguration en utilisant la méthode numérique développée. Dans la partie expérimentale, nous effectuons une série de tests en soufflerie pour observer la limite de stabilité et les différents modes de flottement et également valider notre méthode numérique avec les données expérimentales. L'approche numérique-expérimentale combinée révèle que la reconfiguration est bénéfique jusqu'à la limite de flottement, tandis que la charge due à la dynamique instable du régime post-flottement dépasse la charge rigide, même légèrement au-delà de la limite de flottement pour de faibles rapports de masse. De plus, le lâcher de tourbillons en aval de la plaque entraîne des vibrations induites par vortex, ce qui est la cause du changement de la dynamique de la plaque d'un mode symétrique à un mode antisymétrique.

ABSTRACT

Trees and plants benefit from flexibility by reducing the aerodynamic loading they face by bending and deforming. Flexibility is thus an advantage, allowing *reconfiguration* and drag reduction. However, it is well-known that flexibility is also at the root of many flow-induced vibration phenomena such as flutter, which can be associated with high dynamic stresses. The goal of this research is to find out whether flutter is limiting the benefits that come from reconfiguration. To this aim, we consider reconfiguration of a flat plate under airflow to imitate the complex reconfiguration of real plants. In particular, we look at the dynamics of a flat plate initially positioned normal to fluid flow and clamped at its centerline. In the numerical part, we develop a large displacement structural solver assuming the Euler-Bernoulli beam representing the motion of plates in two dimensions. We use an in-house CFD code for the simulation of the flow field. We employ an iterative partitioned technique to couple the structural and fluid solvers to ensure convergence of the flow and structure variables at the interface level. Further, we study flutter characteristics in a reconfiguring beam using the developed numerical method. In the experimental part, we perform a series of wind tunnel tests to observe the stability limit and different flutter modes and also to validate our numerical method with the experimental data. The combined numerical-experimental approach reveals that the reconfiguration is beneficial up to the flutter limit, while the loading due to unsteady dynamics of the post-flutter regime exceeds the rigid loading for low mass ratios. In addition, the vortex shedding downstream of the plate leads to vortex-induced vibrations, which is the cause of the change in plate dynamics from a symmetrical mode to an anti-symmetrical mode.

TABLE OF CONTENTS

LIST OF TABLES

LIST OF FIGURES

LIST OF ABBREVIATIONS

FSI   Fluid-Structure Interaction

CSS   Conventional Serial Staggered

IIS   Improved Serial Staggered

RANS   Reynolds-averaged Navier–Stokes

URANS Unsteady Reynolds-averaged Navier–Stokes

VIV   Vortex–Induced Vibration

ALE   Arbitrary Lagrangian–Eulerian

CHAPTER 1   INTRODUCTION

In practical engineering applications, structures are mostly rigid and do not deform significantly under loading. Therefore, engineers use the classical theory of elasticity which assumes small deformation in the structures. However, large deformation exists in soft structures in nature. One example of the interaction of fluid and flexible structures in nature is streamlining of flexible plants under wind or water flow. This mechanism helps plants to reduce the drag and withstand harsh environments.

While plants resist the loading by large deformation, the interaction of the fluid and structure might lead to a dynamic instability called flutter, where the structure begins flapping. Flutter is avoided in engineering applications because of the severe consequences to the system, such as possibly loss of the structural integrity. In plants, the adverse effects can permanently change their shape and the growth rate.

Complex shapes of the plants prevents fundamental understanding of the plant's deformation and stability, but simplified geometries allow identifying and weighting the role of different components. Thus, it is essential to develop accurate and viable models to describe the large deformations and nonlinear aeroelastic coupling. This is the motivation of our work. We introduce reconfiguration in the next section. This is followed by presenting available mathematical and physical models in the literature.

CHAPTER 2   LITERATURE REVIEW

2.1   Reconfiguration in Plants

Plants are known to deform when a strong wind is blowing in order to reduce the drag force. This mechanism is termed *reconfiguration* in the literature (Vogel, 1989). For a rigid body, one way to show the Drag force D is through using the Drag formula:

$$D = \frac{1}{2}\rho U_\infty^2 C_D A, \tag{2.1}$$

where ρ is the fluid density, U_∞ is the flow velocity, C_D is the drag force coefficient and A is the frontal area of the rigid body. However, this formula is not valid for a flexible structure. For instance, tuliptree leaves tend to reconfigure to reduce the frontal area, therefore lessen the drag (figure 2.1). To compare the drag force in flexible and rigid structures, Vogel (1984) introduced an exponent ν to account for the reduction in the drag force and flexibility:

$$D \propto U_\infty^{2+\nu}. \tag{2.2}$$

This exponent is a measure of the reconfiguration and mainly negative for plants; the more negative the value, the more drag reduction of the flexible structure, which indicates that the drag force increases sub-quadratically for flexible plants.

10 m/s   15 m/s   20 m/s

Figure 2.1 A tuliptree leaf reconfigures in an increasing wind speed (Image from Vogel 1989)
.

Inspired by reconfiguration of plants, we look at studies conducted on the drag reduction and stability of slender structures as simplified geometries for the complex shape of the leaves

and plants.

2.2 Stability of Slender Structures

Slender structures are ubiquitous in nature and in engineering. In general, if one of the dimensions of the structure is much larger than the other dimensions, then the structure is considered as a slender structure. Examples are beams, plates and shells.

Traditionally in aeroelasticity, the unstable case is divided into two subcategories: static instability and dynamic instability (Hodges and Pierce, 2011). In a static instability case such as divergence, linear theory predicts the amplitude increases to infinity in an exponential fashion. However, in a dynamic unstable case, the amplitude of oscillation increases harmonically. Flutter, as a dynamic instability, arises from the competition of destabilizing aerodynamic forces and stabilizing rigidity of structures. Linear vibration theory can predict the *onset* of instability, but only nonlinear vibration theory is able to describe the motion of the structure after the occurrence of instability (Paidoussis, 2013).

Mainly, we focus on two simple geometry in this project: Axial beam or flag, where the direction of the fluid flow is parallel with the flag, and normal beam, where the fluid flow is perpendicular to the structure. The stability of theses two geometries is discussed in the next two sections.

2.2.1 Axial Beam

Axial beam or conventional flag is a canonical example of fluid structure interactions. It consists of a rectangular plate where the leading edge is fixed in the space and the rest of plate is free to vibrate. Figure 2.2 shows the axial beam configuration, where fluid velocity U is in positive X direction and the plate can vibrate in Y direction. When the flag is subjected to the fluid flow, at lower fluid velocity it remains parallel to the fluid flow, up to a certain velocity when it starts flapping. In accordance with the literature on reconfiguration (de Langre, 2008; Gosselin *et al.*, 2010) and flag fluttering (Michelin *et al.*, 2008b), we define
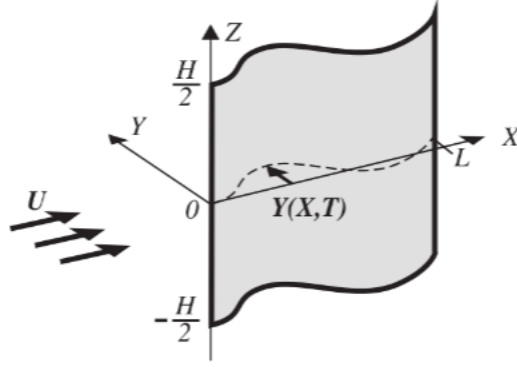
Figure 2.2 Axial beam configuration in fluid flow (Image from Eloy *et al.* 2007)

reduced velocity and mass ratio respectively as

$$U^* = U_\infty L \sqrt{\frac{m_s}{B}}, \tag{2.3}$$

$$M^* = \frac{\rho_f L}{m_s}, \tag{2.4}$$

where U_∞ is the free-stream velocity, m_s is the mass per unit length and width of the beam, ρ_f represents the density of fluid, and L is the length and B is the flexural rigidity of the axial beam. Physically, reduced velocity presents the ratio of the time scale of the natural vibration of the flag to the convective time scale of the flow passing over the flag. The second normalized parameter, mass ratio, shows the importance of fluid to structure inertia forces.

In addition to these parameters, the Cauchy number C_Y is also used as the ratio of bending forces to the stiffness of the structure:

$$C_Y = \frac{\rho_f U_\infty^2 L^3}{B}. \tag{2.5}$$

Eloy *et al.* (2008) considered the flutter instability of a flexible plate in an axial flow numerically and experimentally. Figure 2.3 illustrates their experimental setup and numerical model. They used vortex line theory along with the small displacement Euler-Bernoulli beam equation to find the critical velocity at which flutter occurs. This linear theory can predict reasonably well the dependency of the critical velocity to the mass ratio and the

different modes of vibration, however nonlinear effects are missing in the prediction of the displacements.
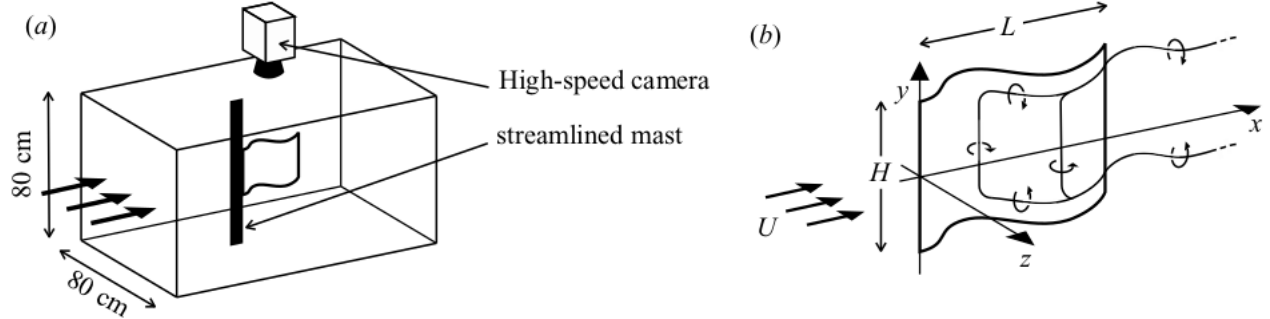
Figure 2.3 (a) The experimental setup and (b) vortex line model used by Eloy *et al.* 2008 to study flutter in a plate (Image from Eloy *et al.* 2008)

A similar approach is employed by Michelin *et al.* (2008b), whereas they used a point vortex model instead of line vortices. For the flow model, a two dimensional potential theory is used. Their model predicts periodic and chaotic regimes depending on the value of the reduced velocity. Figure 2.4 shows three modes of the oscillation predicted by the model of Michelin *et al.* (2008b), where the axial beam is claped at origin. They observed that for low reduced velocity, the flag goes back to its rest position after the initial perturbation and the energy is dissipated by the fluid flow. For intermediate values of reduced velocity, the dynamics converges to a limit cycle oscillation. As the reduced velocity increases, the flag behaves chaotically, and Michelin *et al.* (2008b) reports snapping events in which the force applied to the flagpole is ten times larger than its value in the periodic regime.

Alben and Shelley (2008b) investigated the flapping flag in an inviscid 2D flow with a vortex sheet model. Above a reduced velocity threshold, the flag goes to a unique unstable state with limit cycle oscillations while below this threshold it goes back to the rest state. Figure 2.5 shows the stability boundary as a function of mass ratio, reported by Eloy *et al.* (2008), Michelin *et al.* (2008b) and Alben and Shelley (2008b). The two models of Eloy *et al.* (2008) and Michelin *et al.* (2008b) predict three lobes for the curves, where the transition of the mode shapes of the vibration occurs. Below mass ratio $M^* \approx 1$, the second mode is

unstable and the flag vibrates on its second mode. However above that value the third mode becomes unstable. The next transition happens at $M^* \approx 6$ form the third to the fourth mode of vibration. The model of Alben and Shelley (2008b) shows only a horizontal stability curve where no transition exists.
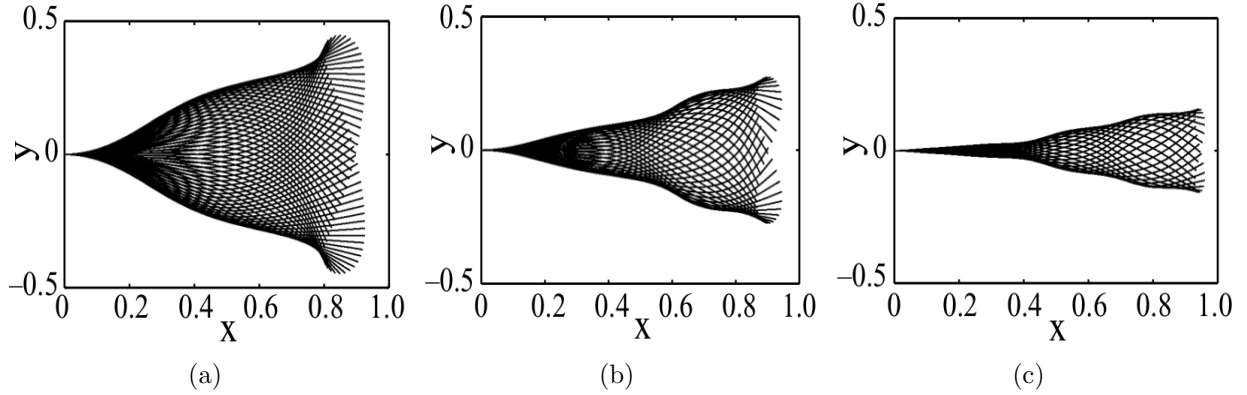
Figure 2.4 Flag vibration modes in Vortex shedding model of Michelin *et al.* (2008b). (a) Second, (b) third and (c) fourth mode shapes of the flag. (Image from Michelin *et al.* 2008b)
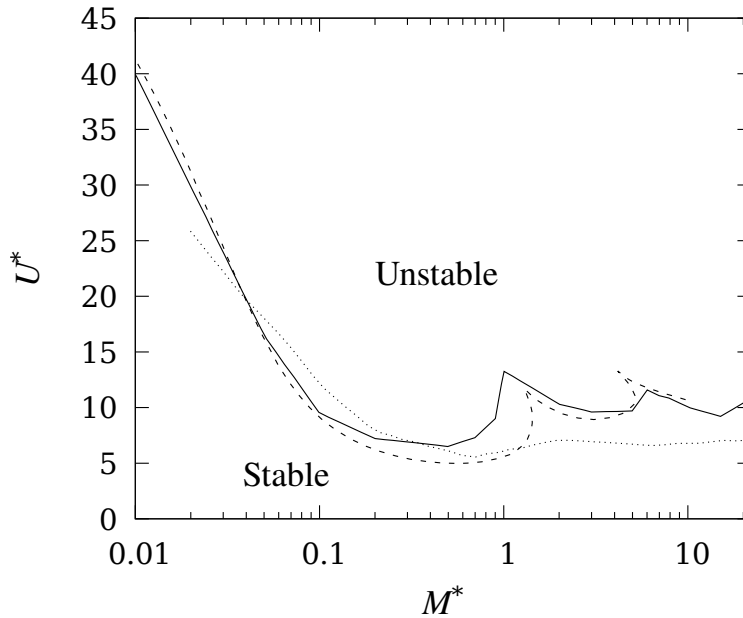
Figure 2.5 Critical velocity for the stability of the flag (stability map), vortex shedding model (Michelin *et al.*, 2008b) (solid), linear stability analysis (Eloy *et al.*, 2008) (dashed), and vortex sheet approach (Alben and Shelley, 2008b,a) (dotted).

Later, Alben (2015) extended their model to a channel-bounded flapping flag. Their study suggest that for heavier flags confinement increases the region of the instability. Also

decreasing the wall spacing changes the flapping to a higher mode. Their model lacks the effect of viscosity in the fluid flow, which may change the effect of wall boundedness on the stability map in cases where the flag interacts with the viscous boundary layer.

Kerboua *et al.* (2008) assessed the impact of fluid on natural frequencies of plates by developing a hybrid finite element–shell theory model of plates coupled with fluid. The plates can be totally submerged or floating on the surface. Their model predicts reduction of the natural frequencies of plates, in good agreement with experimental data.

Abderrahmane *et al.* (2011) used 2D filaments to observe the dynamics of an axial beam in soap-film experiments. They show that the flapping is quasi-periodic, where the main flapping oscillation is altered by small-amplitude, small-frequency components. Interestingly, they did not capture the periodic flapping. Another important observation was that the flag continuously switches between straight and flapping states. Tang *et al.* (2009) analyzed the energy transfer between the fluid flow and the plate, and introduced the flutter-mill concept in order to generate electrical power from the flapping motion. Despite the compact size of the flutter-mill, it showed a promising performance compared to conventional wind turbines. In the following study, Zhao *et al.* (2012) used Poincaré maps, phase-planes and time-traces to characterize the motion of the system. They predicted the flutter boundary numerically and experimentally, and investigated the effects of the aspect ratio—defined as the ratio of width to length of the plate. They could observe hysteresis effects on high aspect ratios, but not low aspect ratio plates.

Eloy *et al.* (2012) studied the discrepancy between the experimental data and the numerical simulation's prediction of the flutter velocity in a flag. The experiments showed a larger gap in flutter velocity observation—the difference between the flag flutter velocity when the wind velocity was increasing from zero to the case when it was decreasing from high velocities, known as the hysteresis effect. They argued that the curvature of the plate or planeity effects are the most probable cause of hysteresis in predicting the critical velocity of the flag instability in experiments.

To study the effect of compressibility, Colera and Pérez-Saborid (2018) used a linearized potential flow with a linear elastic beam equation model for the plate. They argued compressibility effects would cause an over-estimation of the flutter speed at Mach number of 0.1. Because nonlinear effects were not included in their model, their results were limited to only calculating the critical velocity and no post-critical behavior could be captured.

Another relevant configuration is the inverted flag, which is similar to the axial beam configuration except for the fact that the leading edge is free to vibrate, and the trailing edge is fixed. According to Tavallaeinejad *et al.* (2020), the developed analytical model of the inverted flag dynamics suggests that the inverted flag turns unstable primarily due to fluidelastic instability, and not flow-induced instabilities such as vortex-induced vibration, though the quasi-steady flow assumption of their aerodynamics model limits the study of vortex shedding impacts.

In the next section, we look at another configuration studied in the literature, where the flat plate is placed normal to the direction of fluid flow.

2.2.2   Normal Beam

Another configuration which is used by researchers to study drag and reconfiguration is the normal beam or a flat plate anchored at its center in three dimensional case. Figure 2.6 shows the normal beam configuration in fluid flow. Normal beam configuration is simple enough to be tested in a wind tunnel and numerical simulations, yet sufficiently complex to allow us to use it as a model to study reconfiguration limits and flutter of flexible structures such as plants.
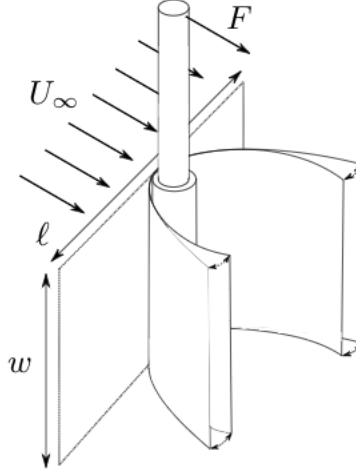
Figure 2.6 Normal beam configuration in fluid flow. The initial, straight shape and the deformed, flapping shape are shown.

Gosselin *et al.* (2010) looked at the reconfiguration of a normal beam using empirical formulation for the drag force and wind tunnel experiments. They described the reconfiguration of the normal beam by dimensional analysis. A simple reasoning showed that drag scales with the flow velocity with a Vogel exponent of −2/3. Also, they stated that a scaled Cauchy number with drag coefficient allows collapsing all the drag measurements in one single curve which confirms the dimensional analysis. In addition, they analysed two mechanisms of the drag reduction in reconfiguring normal beam, and showed that the reduction of the projected area and the streamlining are the two mechanisms of drag reduction. According to Gosselin *et al.* (2010), as long as the free ends of the normal beam are bending toward the downstream, both mechanisms help drag reduction. However, when the free ends of the normal beam are parallel to the flow, the drag reduction is solely due to projected area reduction.

A similar arrangements of plates was examined by Schouveiler and Eloy (2009). They experimentally studied coupled flutter modes of two, three and four plates parallel to the fluid flow, and compared the outcomes with predictions of linear stability analysis. Figure 2.7 shows two parallel plates flapping in their experimental study. They mentioned that above a critical value of the flow velocity, the plates begin to flutter symmetrically in a mode that they referred to as varicose mode (figure 2.7 a). When flow velocity is further increased,

a second mode is observed in which the plate flapping occurs in-phase. This mode is termed as sinuous mode (figure 2.7 b). Transition of modes in two parallel plates was discussed by Si-Ying *et al.* (2013) as well. Although they report the same in-phase and out-of-phase modes in their experiments, the mechanism of transition remained as an indeterminate problem. Recently, Leclercq *et al.* (2018) used a reduced-order model to understand drag reduction in flexible beams. Their reduced model consists of adding two external forces as the effect of the flow on the structure: the added mass force due to the potential component of the flow, and a drag force due to the flow separation. They could identify three distinct regimes: static (S), periodic (P) and a non periodic (NP) or chaotic regime (figure 2.8). As wind velocity increases, the normal beam bends and aligns with the fluid flow. At reduced velocity $u \approx 17$, the static regime ends and a regular, periodic flapping of the flag is observed. Figure 2.8 shows that the period regime ends at $u \approx 64$ and the flapping is no longer periodic. Their study suggests that except for some snapping events, flutter does not limit drag reduction by reconfiguration. We address this issue in the post-critical flutter regime section.
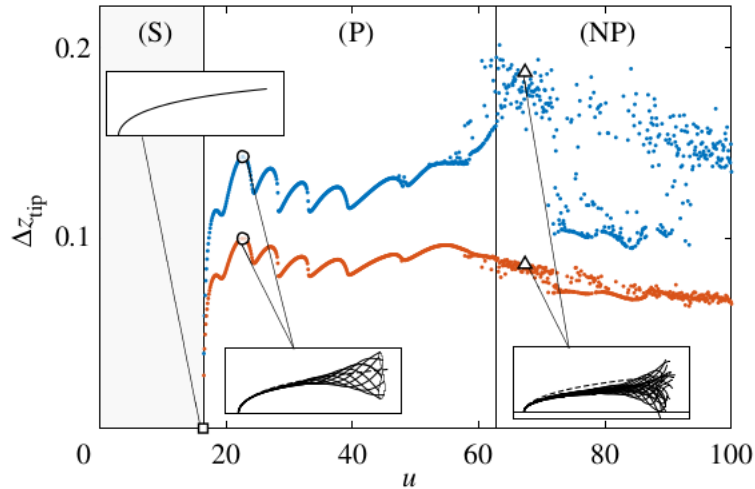
Figure 2.8 Vertical amplitude of the flag tip (blue) and the standard deviation (orange) versus reduced velocity. Three regimes of static (S), periodic (P) and a non periodic (NP) flag flutter exist. (Image from Leclercq *et al.* 2018)
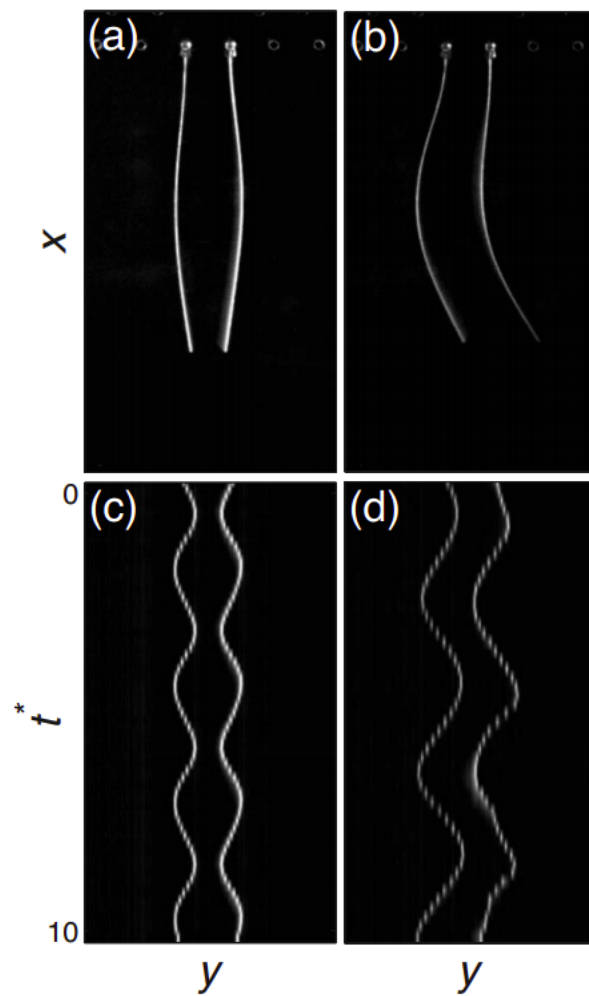
Figure 2.7 Visualization of (a) the varicose mode and (b) sinuous mode coupled flutter of two plates (flow from top). (c) and (d) show the corresponding space-time diagrams. (Image from Schouveiler and Eloy 2009)

2.3 Vortex Induced Vibration in Normal Beam Configuration

Study of the fluid-structure interaction of bluff bodies reveals that vibrations can occur due to the vortices in the wake region. In motionless solids, vortices are shed downstream of the body due to the shear layer instability in the boundary layer, with vortex shedding frequency proportional to the flow velocity (De Langre, 2006). If the frequency of the vortex shedding equals the natural frequency of the bluff body, then *lock-in* occures, which significantly changes the dynamics of the fluid structure interaction.

In case of non-deformable structures, vortex induced vibration is well studied in the literature. For example, De Langre (2006) used a linear wake oscillator model to study lock-in mechanism. This model reproduces the range of lock-in for a cylinder in very good agreement with experimental data. However, in continuous systems, when several modes contribute to the motion of the system, the interaction of the frequencies of the motion and the wake frequency in the lock-in process becomes very complex.

Zhu (2007) performed simulation on a geometry similar to the normal beam to investigate the influence of Reynolds number (range 30-800), dimensionless flexural rigidity and dimensionless fibre length on vortex shedding using the immersed boundary method. He pointed out that while all these parameters change the structure of vortices, Reynolds number has little influence on the frequency of vortex shedding in the given range. He was unable to investigate the impact of the Reynolds number of higher than 800 due to inaccuracy of the immersed boundary method.

Miller *et al.* (2012) used two types of flexible structures , a cone and a flat plate, as simplified model for leaves to study reconfiguration with a 2D numerical setup and water tunnel tests. As a result of using flexible tethers to connect the models in their experiments, they observed larger forces and stronger vortex shedding in the range of their simulations.

We expect that, for the configuration of the normal beam, the interaction of vortex induced vibrations and flutter to alter the boundary of the stability map. This issue is reported in the previous work of Sansas (2016) where he had to use a coarse grid to damp out the vortices

by numerical dissipation to simulate reconfiguration of the normal beam. In addition, the interplay of theses two phenomena will unveil a very rich dynamics of fluid and structure motions.

2.4   Post-critical Flutter Regime Dynamics

Drag reduction due to reconfiguration is known to help biomechanical organisms withstand harsh environments. However, modulation of the drag force due to post-critical kinematics could be the source of structural failure in flexible structures.

Leclercq *et al.* (2018) devoted a section of their research to study the post-critical regime of a half normal beam configuration. They focused on the impact of slenderness and mass ratio on the kinematics, and variation of drag in the post-critical regime. Solving the full time-dependent nonlinear equation of motion for the beam with added reduced order fluid forces, they concluded that slenderness prevents chaotic motion in high flow velocities. Figure 2.9(a) shows tip displacement becomes non-zero when periodic flapping happens at $u \approx 20$. The periodic flapping exist for higher reduced velocity up to $u \approx 60$ where the chaotic regime begins. However, at $u \approx 80$, the motion of the structure becomes periodic. In addition, They stated that reducing the mass ratio (heavier structure) leads to larger amplitude of vibration and earlier onset of flutter (figure 2.9(b)).

(a) (b)
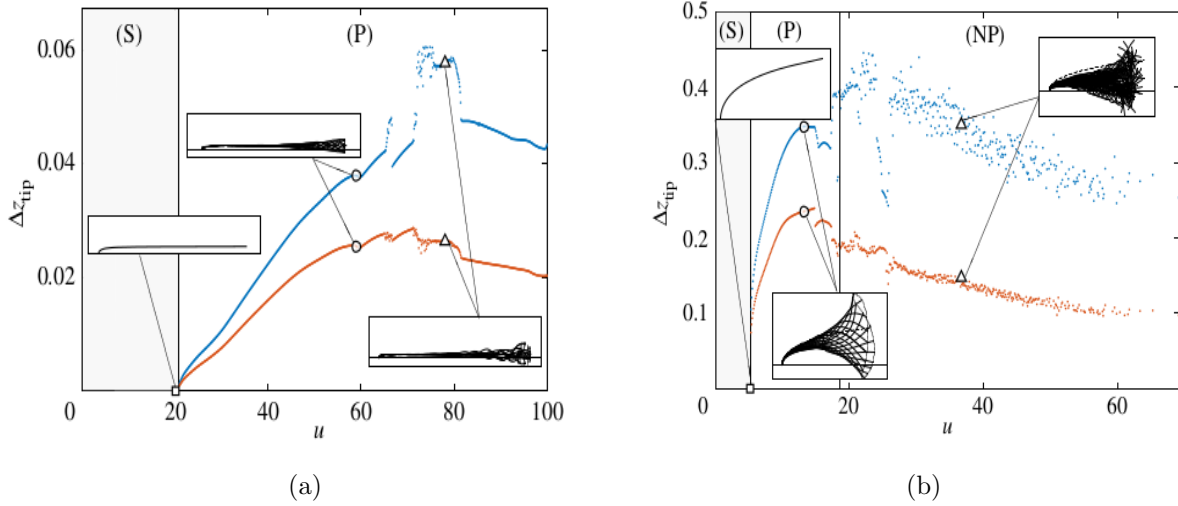
Figure 2.9 Normal beam flutter amplitude (blue curve) versus reduced velocity. Orange curve shows the standard deviation of the amplitude in time. (a) In high reduced velocity, flapping motion goes back to periodic regime (b) Reducing mass ratio causes larger amplitude vibration and early flutter (Image from Leclercq *et al.* 2018).

Following the work of Gosselin *et al.* (2010), Leclercq *et al.* (2018) used reconfiguration number R to measure the ratio of the drag in the deflected structure D compared to the rigid, straight case D_{rigid}:

$$\mathcal{R} = \frac{D}{D_{rigid}}. \tag{2.6}$$

Figure 2.10 shows reconfiguration of a deforming structure, half of the normal beam, as a function of Cauchy number. When $C_Y \lesssim 1$, the structure is not deformed considerably and $\mathcal{R}$ remains near one. As Cauchy number increases and structure deforms, $\mathcal{R}$ reduces to below one which implies that the experienced drag by the deformed structure is less than the rigid structure. Further increase of the Cauchy number leads to flutter instability and periodic flapping. Although the drag increases once flutter happens in the periodic (P) regime compared to the static deformation, it still remains less the the rigid case.

They argue that for most cases, the total drag induced by flutter is below the rigid drag, which means the reconfiguration number is remains below unity. However, for lower mass ratios, the large-amplitude flapping may increase the total dynamic drag beyond the static

value. Nevertheless, the study of the impact of mass ratio on flutter-induced drag remains incomplete. The limitation of their work includes the absence of vortex shedding—due to using a simple reduced-order model, and experimental validation.

In a closely related work, Leclercq and de Langre (2018) extended their model to an oscillatory fluid flow. Applying the same model as Leclercq *et al.* (2018), they identified four kinematic regimes of rigid, modal, convective and large amplitude in amplitude-frequency space. In all cases, the reconfiguration number is below one, except for cases where the frequency of flow matches one of the natural frequency of structure. Their findings are valid for the cases where the inertia of the structure is negligible (or equivalently high mass ratios) which permits neglecting the displaced mass by structure. They predicted that the inclusion of the structural inertia may significantly change the output of their work, and more complicated dynamical behavior come into play.

2.5 Numerical Methods in Fluid-Structure Interaction

In this section we introduce a brief review of the numerical issues found in fluid-structure interaction. Textbooks such as Blazek (2015), Bathe (2006) and Versteeg and Malalasekera (2007) provide detail of the methods in fluid and solid dynamics separately. Here we focus on the topics appearing in the coupling of the fluid and the structure domains.

2.5.1 Coupling Approaches in Fluid-Structure Interaction

As an example of a multiphysics problem, solving a Fluid-Structure Interaction problem requires an efficient and robust strategy to find the solution of the coupled domains. Many questions arise in the coupling of the fluid and solid domains such as stability, consistency and conservation properties of the coupling method. Mainly, the coupling approaches are referred as partitioned and monolithic, however, other labels such as strongly/weakly coupled, fully/loosely coupled and explicit/implicit exist in the literature. We use partitioned and monolithic to categorize these approaches.
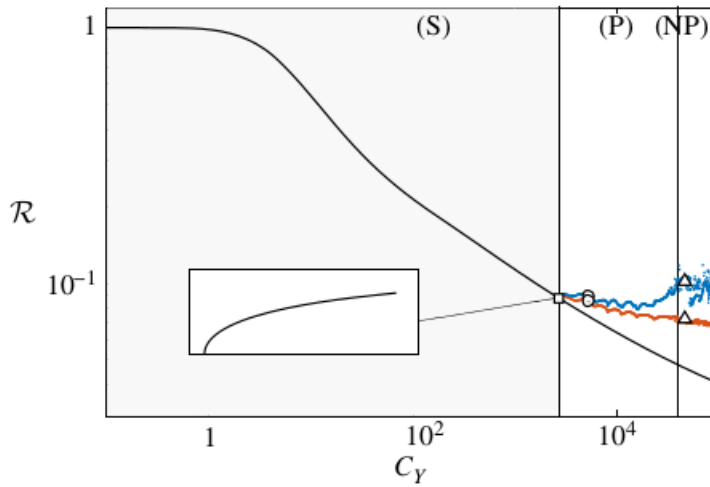
Figure 2.10 Time averaged (orange) and maximum (blue) reconfiguration number versus Cauchy number of the half normal beam configuration. The static reconfiguration curve is shown in black. (Image from Leclercq *et al.* 2018).

The partitioned method is appealing since it uses existing codes with minimal changes. However, this advantage comes at a very severe cost: stability. If we define generally nonlinear operators of $f = F(d)$ and $d = S(f)$ for the fluid and structure solvers, and d and f as displacements and forces for the inputs and outputs, the simplest partitioned method which only solves the domains sequentially in time t is shown in figure 2.11:
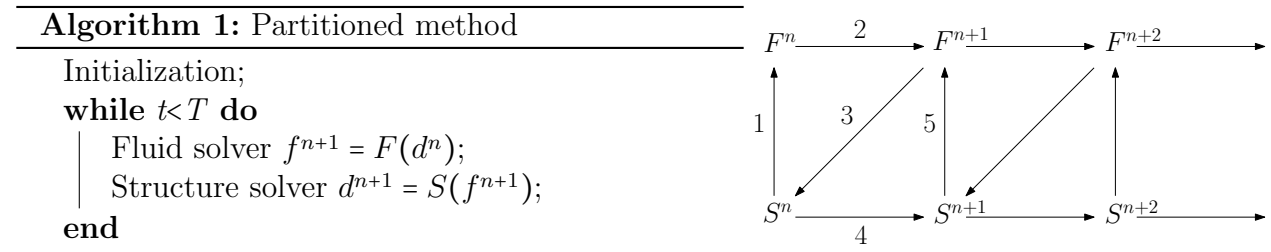
Figure 2.11 Simplest partitioned method

Farhat and Lesoinne (2000) reviewed the partitioned methods in coupled fluid-structure problems. They refer the simple partitioned method as *Conventional Serial Staggered* (CSS) procedure. They proved that even by using higher order schemes in time discretization of both solvers, the CSS is at most first order accurate. So apart from the limitation set by the desired accuracy on time step, a more restrictive limit is set by the explicit nature of

the CSS method (CFL condition). Farhat and Lesoinne (2000) proposed a new method called *Improved Serial Staggered* (ISS) to remedy the first order accuracy by advancing fluid and structure solvers with a half time step delay. But explicit treatment of this partitioned method still retains the stability issue. In addition, satisfying the conservativeness of the energy is not tested in this approach.

The stability of the partitioned approach is highly dependent on the flexibility of the structure. Due to the complexity of the full fluid-structure problems, some researchers attempted to analyze the stability issue by looking at model problems. Piperno *et al.* (1995) presented a family of implicit/explicit partitioned procedure and discussed accuracy, stability, heterogeneous computing, subcycling and parallel processing for a one dimensional piston model problem. In the second part, Piperno and Farhat (2001) evaluated the energy that is created numerically at the fluid/structure interface in the partitioned approach. They validated their algorithm by solving the two and three dimensional, transonic and supersonic wing and panel flutter. They introduced n^{th}-order energy accurate partitioned procedure concept, and they have shown that the simple partitioned approach is at most first-order energy accurate. The piston model problem is a case that is studied by other researches as well. For examples, look at (Piperno, 1994), (Blom, 1998) and (Lefrançois and Boufflet, 2010).

2.5.2 Iterative Partitioned Approach

Vierendeels *et al.* (2011) investigated the stability issue of the partitioned approach with applications in the biomechanical field. They showed that, in certain conditions depending on the geometry and the ratio of solid to fluid densities, the simple partitioned method is *unconditionally unstable*. In other words, unlike many situations in numerical simulations, decreasing the timestep cannot make the scheme stable.

In order to solve the stability issue of a simple partitioned method, we can use an iterative partitioned algorithm. The composition of the solid $d = S(f)$ and fluid $f = F(d)$ operators in a single operator $d = SoF(d)$ reduces the simple partitioned approach to a fixed-point

iteration form based on the interface displacement:

$$d^{n+1,k+1} = SoF(d^{n+1,k}), \tag{2.7}$$

where n is the timestep and k is the iteration counter. All the fixed-point iteration methods such as Gauss-Seidel or Jacobi can be used to find the solution. Furthermore, the partitioned approach can be written in root finding form:

$$R(d^{n+1}) = d^{n+1} - SoF(d^{n+1}) = 0, \tag{2.8}$$

$$d^{n+1,k+1} = d^{n+1,k} - J^{-1}(d^{n+1,k})R(d^{n+1,k}), \tag{2.9}$$

where $J^{-1}(d^{n+1,k})$ is the inverse of the Jacobian matrix. Then a Newton-Raphson method is applied to the problem. But the computation of the Jacobian matrix for this system is usually expensive, if possible. Thus another group of methods emerge that approximate the Jacobian which are called quasi-Newton methods. The superiority of fixed-point iteration methods or Newton methods is not *a priori* and is problem dependent; generally fixed-point iteration methods benefit from less computational time per iteration while they require more iterations than Newton methods to reach the desired accuracy. In some cases with strong interaction in the physics of the problem, Newton methods perform better than fixed point iteration methods. These iterative partitioned approach can achieve the same solution as monolithic approach with sufficient iterations and accuracy. Degroote *et al.* (2008) mentions that for an internal flow in a tube, the number of coupling iterations increases when the structure becomes more flexible or the timestep is decreased.

The complete iterative partitioned approach consists of a Predictor $d^k = P(d^n, d^{n-1}, ...)$ to estimate the initial guess for the next subiteration, and a relaxation factor ω to stabilize the subiterations is shown in figure 2.12:

Algorithm 2: Iterative partitioned approach

Initialization;

while $t < T$ **do**

    Predictor $d^k = P(d^n, d^{n-1}, ...)$;

    while $k < iter_{max}$ **do**

        Fluid solver $f^{k+1} = F(d^k)$;

        Structure solver $d^{k+1} = S(f^{k+1})$;

        if $|d^{k+1} - d^k| < tol$ **then**

            $d^{n+1} = d^{k+1}$;

            break;

        else

            $k = k + 1$;

        end

        Relaxation $d^{k+1} = w_k d^{k+1} + (1 - w_k)d^k$;

    end

end
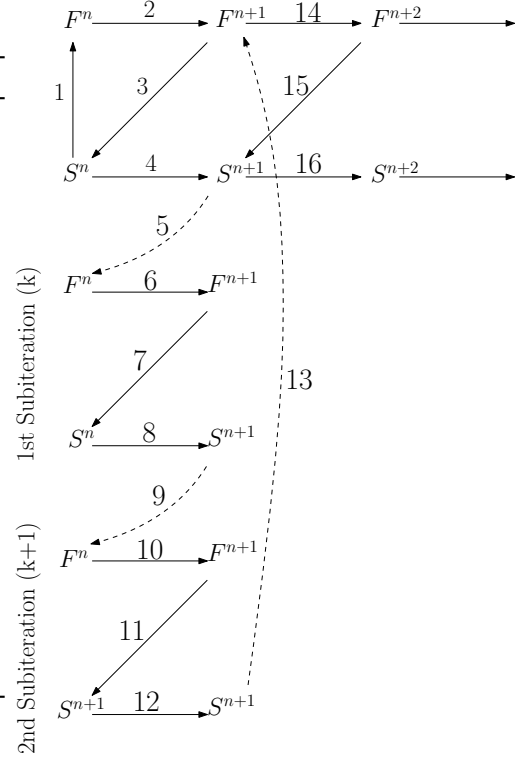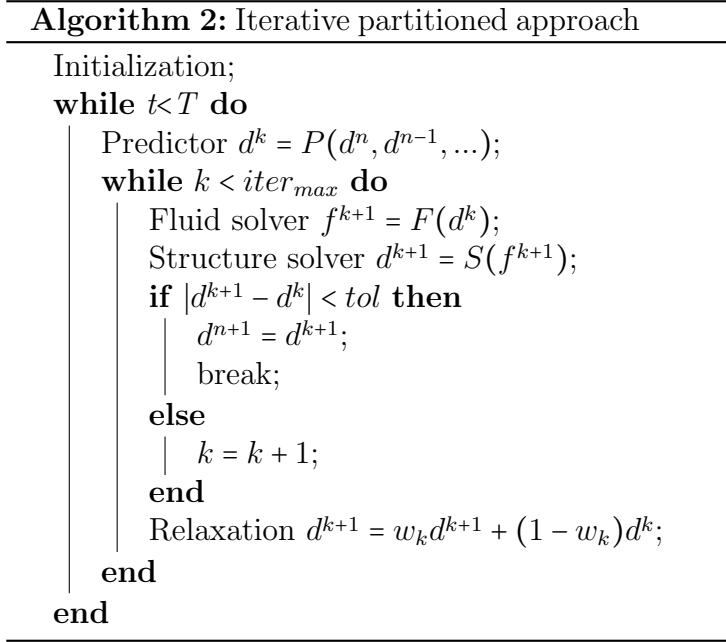
Figure 2.12 Iterative partitioned approach

Aitken dynamic relaxation (w_k) is proposed by Küttler and Wall (2008) to accelerate the convergence of the sequence of displacements in the subiterations:

$$w_k = \frac{(d^{k-1})^T (d^k - d^{k-1})}{\|d^k - d^{k-1}\|^2}. \tag{2.10}$$

Michler *et al.* (2004) compared simple partitioned and iterative partitioned approaches for one-dimensional piston model problem. By defining the ratio of accuracy to the computational cost as a measure of computational efficiency, they concluded simple and iterative partitioned approaches have comparable computational efficiency in a simple one-degree-of-freedom structure model. However, they expected superior efficiency of an iterative partitioned approach in case of multiple mode problems.

Although using an iterative partitioned approach cures the stability problem of a simple partitioned approach which is due to explicit time integration, the inherent iterative nature of the iterative partitioned approach introduces another problem. Unfortunately, the iterative

partitioned approach is not always converging. In an interesting article, Joosten *et al.* (2009) analyzed the block Gauss-Seidel procedure in a model problem of mass, springs and dashpots. Their results demonstrate that the convergence of the block Gauss-Seidel procedure depends on the mass ratio and stiffness ratio of the two domains. In an asymptotic regime when the time step tends to zero, the stability solely depends on the mass ratio.

In mathematical terms, the stability of an iterative method depends on the spectral radius of the iteration matrix, which is the largest eigenvalue of the iteration matrix. The iterative method can converge if and only if the spectral radius of the iteration matrix is less than one. The spectral radius depends on the scheme that is used to solve the equations, and also the parameters of the problem that is solved by the iterative method. Therefore, changing the parameters of the problem such as mass ratio or flexibility of the structure, may lead to a spectral radius of greater than one and subsequently divergence of the iterative method.

Von Scheven and Ramm (2011) addressed sensitivity of numerical schemes to the interaction of slender structures and incompressible flows. They compared block Gauss-Seidel iteration and Newton-Krylov techniques in iterative partitioned approach applied to a three dimensional flexible plate attached to a rigid square cylinder. This problem is basically an extension of Wall (1998) benchmark to 3D. They argued that using a coarser grid as a predictor to the fine grid solution of the iterative method would reduce the computational time by 30%. Additionally, neither of block Gauss-Seidel iteration and Newton-Krylov techniques are always superior in all the cases in terms of overall computational efficiency.

Joosten *et al.* (2009) also showed that inclusion of a constraint to one of the subsystems leads to divergence of the iterative method, which happens in realistic FSI applications. For instance, in coupling an incompressible flow with a flexible structure, the incompressiblity of the flow is a constraint which deteriorates the convergence. This phenomena is termed *added mass* effect, which was the topic of numerous research on convergence of FSI simulations.

2.5.3 Added Mass Effect

In aeroelasticity applications, partitioned approach is used frequently without difficulty. In this case, a rigid wing is interacting with a low density fluid flow. As a result, the fluid to solid density ratio is low. When the wing vibrates, it accelerates the flow around the wing which can be interpreted as an additional mass added to the structure. Because the ratio of the fluid to structure density is low, the added mass will not cause an instability issue in the partitioned approach (Breuer *et al.*, 2012).

However, added mass effect is known to be a source of difficulty in other cases of numerical FSI. Causin *et al.* (2005) provided a mathematical explanation of numerical instabilities in partitioned approach for a simplified fluid-structure interaction problem of the blood flow in human arteries. They observed convergence problems in the following two cases, which are common in interaction of incompressible flows with thin structures:

- when the density of the structure is lower than a threshold;

- when the domain has a slender shape and the length of domain is greater than a threshold.

In theses cases, partitioned method showed unstable behavior and iterative partitioned method required a high number of subiterations for convergence. In addition, they showed that using a relaxation to stabilize the coupling is not always practical because there is a maximum value for the relaxation depending on the parameters of the problem. When the spatial discretization is refined (consistent case), the relaxation parameter tends to zero, so the use of relaxation parameter is not practical.

In another study, Van Brummelen (2009) compared added mass effects in incompressible and compressible flows. By examining a semi-infinite fluid flow interacting with a flexible panel, they showed an iterative partitioned approach can be stabilized only for sufficiently small timestep for compressible flows. On the other hand, the iterative partitioned approach can remain unstable in some cases for the incompressible flows even with using

smaller timestep. In other words, using a simple model Van Brummelen (2009) showed an iterative partitioned approach is unconditionally unstable for an incompressible flow, and it is conditionally stable for a compressible flow. So still there is a limit on the timestep value even in a compressible fluid flow model.

2.5.4   Monolithic Approach

In a monolithic approach, both fluid and structure part are solved in a single matrix of solution variables. This could happen by using different discretization methods for the separate domains, or using the same discretization. As a result, a new code is necessary to be developed for the desired problem which is against the modularity rule from industrial software engineering perspective. However, the problems associated with convergence in partitioned numerical FSI will disappear.

Hübner *et al.* (2004) used velocity variables for an incompressible fluid flow interacting with a geometrically nonlinear structure and applied stabilized space-time finite element method to the both domains to get a single system of equations. They mentioned that formulating the problem in one system of equation may lead to ill-conditioned system matrices, and also finding an appropriate preconditioner is not a trivial task. Using a monolithic approach, they achieved convergence of the system of equations within two to four fixed-point iterations even in strong interactions with large deformation of the structure.

2.5.5   Conclusion

The existence of many numerical schemes and the dependency of the efficiency and robustness of the method on the problem make it quite difficult to compare the coupling approaches in fluid-structure interaction. We present a general overview of the discussed methods in previous sections in table 2.1. We define efficiency as the ratio of the accuracy to the computational cost where 5 means the best and 1 the worst efficiency. The efficiency is shown in cases when there is a strong interaction in the physics of the problem. We also compare the

implementation of theses methods, where 5 is the easiest and the most modular method and 1 is the most difficult and the least modular method.

Table 2.1 A summary of the coupling approaches

Coupling approach	Stability issues	Efficiency	Implementation
Partitioned	unconditionally unstable in some cases	1	5
Iterative Partitioned	high number of subiterations and unstable in strong interactions	2	4
Partitioned with added compressibility	compressible flows still suffer from stability issues	3	3
quasi-Newton	the most robust partitioned method	4	2
Monolithic	can result in ill-conditioned iteration matrix	5	1

CHAPTER 3   PROBLEM STATEMENT

3.1   Problem Identification

The studies reviewed in chapter 2 vary in the level of the approximation from modeling linear elasticity and small displacement for the structure and linearized Euler equation and potential theory for the flow, to higher fidelity models of the nonlinear elasticity and Reynolds-averaged Navier–Stokes equations. Although past studies addressed many issues in the fluid-structure interaction problem of slender structures, the answer to the following questions is missing in the literature:

- Can flutter limit reconfiguration? How does flutter affect the reconfiguration of beams and plates that are placed under fluid flow with different configurations?

- Can flutter, vortex-induced vibration and reconfiguration all happen in a single, simple system of a reconfiguring beam?

- What is the influence of mass ratio on beam reconfiguration?

3.2   Objectives

The general objective of this research project is to analyze the flutter instability in reconfiguring beam using high-fidelity numerical simulations and wind tunnel tests. The specific objectives of the proposed research project are:

1. To implement a partitioned FSI approach in order to determine the onset of flutter instability and drag reduction due to reconfiguration in flapping flags considering nonlinearities in the structure and fluid model;

2. To illustrate the dynamics of flutter and vortex induced vibration, the range of interplay, and their impact on the boundary of the stability of a reconfiguring beam;

3. To inspect the post-critical flutter regime, and look at the modulation of the dynamic drag and reconfiguration in post-critical regime.

Obtaining the onset of flutter possesses several challenges. One of them is to distinguish between the instability due to the physics of the problem and unwanted oscillation attributed to poor convergence of the numerical simulations. Using partitioned method reduces the time required for development of the FSI code, While the consequences are possible numerical instability, and the accuracy dictated by the lowest accurate module in the portioned simulation, and also the accuracy of data transfer between different modules. Another challenge is that the allowed timestep is restricted by the solver type, the computational geometry, and the fluid and solid properties. Generally lighter and less stiff structures need smaller timestep for the simulation.

Normal beam configuration is similar to a bluff body, and prone to vortex-induced vibrations. For instance, one of the issues encountered in the previous work of Sansas (2016) was interaction of vortices with motion of the structure, which resulted in large vibration of the structure and divergence of the code. Owing to the fact that Sansas (2016) solvers were only weakly coupled, Sansas (2016) had to numerically damp out the vortices. Work of Zhu (2007) showed that theses vortices can only cause small amplitude vibration in the normal beam configuration. But limited range of the Reynolds number and using a cartesian grid with immersed boundary method make it difficult to extend their conclusions.

Although the review of the work of Leclercq *et al.* (2018) in chapter 2 showed that flutter almost never undermines the ability of reconfiguration to reduce drag, their study is done by a reduced-order model for fluid flow forces, and they did not validated their model against experimental data. Moreover, their analysis on the effect of the mass ratio is incomplete.

CHAPTER 4   METHODOLOGY

4.1   Strategy

In order to investigate the underlying mechanisms of flutter, we combine experimental and numerical approaches. In the former, we perform wind tunnel tests on slender, highly flexible structures such as rectangular plates clamped at its center. In the latter, we implement an in-house coupled fluid-structure interaction code. The code couples a compressible Unsteady Reynolds-Averaged Navier–Stokes (URANS) solver for the fluid flow with a geometrically nonlinear Euler-Bernoulli beam model. The details of the numerical and experimental methodologies are described in this chapter.

4.2   Numerical Framework

4.2.1   Fluid Governing Equations

To account for the deformation of the fluid domain by the structure motion, we solve the URANS equations with a moving grid technique, i.e., we solve an Arbitrary Lagrangian Eulerian (ALE) formulation of the Navier-Stokes equations. Accordingly, the convective fluxes are modified with the mesh velocity. For a moving control volume Ω bounded by the closed surface ∂S with a surface element dS, the time t dependent integral form of the Navier–Stokes equations are expressed as follows (Blazek, 2015):

$$\frac{\partial}{\partial t} \int_{\Omega} \mathbf{W} d\Omega + \int_{\partial \Omega} (\mathbf{F}_c{}^M - \mathbf{F}_v) \cdot d\mathbf{S} = 0, \tag{4.1}$$

where $\mathbf{W}$ is the vector of conservative variables: $\mathbf{W} = [\rho, \rho u, \rho v, \rho E]^T$, ρ denotes density, u,v the Cartesian velocity components, E total energy per unit mass. The modified convective

flux $\mathbf{F}_c^M$ and viscous flux $\mathbf{F}_v$ are written as

$$
\mathbf{F}_c^M =
\begin{bmatrix}
\rho V_r \\
\rho u V_r + n_x p \\
\rho v V_r + n_y p \\
\rho H V_r + V_t p
\end{bmatrix}
\quad
\mathbf{F}_v =
\begin{bmatrix}
0 \\
n_x \tau_{xx} + n_y \tau_{xy} \\
n_x \tau_{yx} + n_y \tau_{yy} \\
n_x \theta_x + n_y \theta_y
\end{bmatrix},
\tag{4.2}
$$

$$
\theta_x = u \tau_{xx} + v \tau_{xy}, \tag{4.3}
$$

$$
\theta_y = u \tau_{yx} + v \tau_{yy}, \tag{4.4}
$$

$$
H = E + \frac{p}{\rho}. \tag{4.5}
$$

where H stands for total enthalpy and p static pressure, n_x and n_y are outward facing unit normal vector of the surface $\partial\Omega$, τ_{xx}, τ_{yy} represent normal stresses in x and y direction respectively, τ_{xy} and τ_{yx} are shear stresses, and θ_x and θ_y are describing the work of the viscous stresses. V_r is the contravariant velocity relative to the grid velocity V_t given by

$$
\mathbf{V}_t = \frac{\partial x}{\partial t}\mathbf{n}_x + \frac{\partial y}{\partial t}\mathbf{n}_y, \tag{4.6}
$$

$$
\mathbf{V} = u\mathbf{n}_x + v\mathbf{n}_y, \tag{4.7}
$$

$$
\mathbf{V}_r = \mathbf{V} - \mathbf{V}_t. \tag{4.8}
$$

In cases where the volume of the cells is changing due to deformation, the Geometric Conservation Law (GCL) must be satisfied to avoid errors induced by deformation of control volumes. It relates the change of the control volume to the surface motion as follows

$$
\frac{\partial}{\partial t} \int_\Omega \mathrm{d}\Omega + \int_{\partial\Omega} \mathbf{V}_t \cdot \mathrm{d}\mathbf{S} = 0. \tag{4.9}
$$

4.2.2 Flow Solver

In order to solve the URANS equations, we use the finite volume compressible flow solver NSCODE developed at Polytechnique Montreal. Using an in-house code allows full transparency and access to all variables and processes. This can be difficult with a black box commercial solver. The NSCODE flow solver has already has been verified and validated through numerous test cases (Lévesque, 2015). The solver uses the Jameson-Turkel-Schmidt (JST) scheme for the convective fluxes and a multistage Runge-Kutta method with dual time stepping for the temporal discretization. For grid generation, we use the structured grid generator NSGRID, also developed at Polytechnique Montreal, which is able to generate high quality meshes with elliptic and hyperbolic algorithms (Hasanzadeh Lashkajani *et al.*, 2015).

4.2.3 Structure Governing Equations

The large displacement of the structure is expressed with the 2D nonlinear Euler-Bernoulli beam equations. Figure 4.1 shows the modelled cantilever beam with the defined curvilinear coordinates and also the forces acting on the element of the beam.
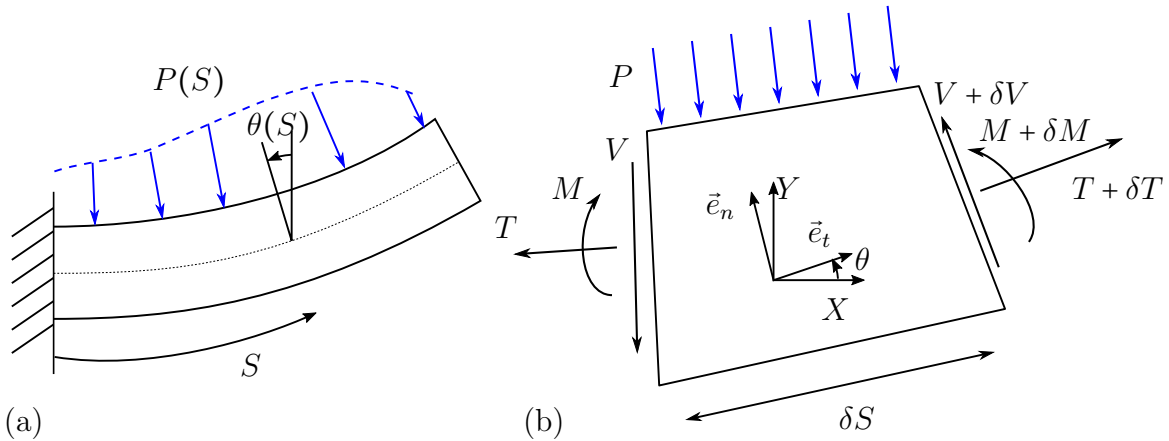
Figure 4.1 Schematics of the modelled cantilevered beam: (a) the whole beam and its curvilinear coordinate; (b) the free-body diagram on a beam element.

The beam is of length L, thickness h, and mass per unit length m. A curvilinear Lagrangian coordinate follows the centre line of the beam from its clamped end at $S = 0$ to its

free end at $S = L$. The bending angle $\theta(S)$ measures the local deformation of the beam. The Lagrangian coordinates are related to the fixed Eulerian coordinates X and Y:

$$\frac{\partial X}{\partial S} = \cos\theta, \quad \frac{\partial Y}{\partial S} = \sin\theta. \tag{4.10}$$

The fluid flow creates a pressure difference $P(S)$ across the thickness of the beam. We consider an infinitesimal beam element of length δS. Its normal and tangent vectors are $\vec{e}_n$ and $\vec{e}_t$, respectively. The summation of forces in these two directions and the summation of moment on the element lead to:

$$-m\frac{\partial^2 X}{\partial t^2}\sin(\theta) + m\frac{\partial^2 Y}{\partial t^2}\cos(\theta) = \frac{\partial V}{\partial S} + T\frac{\partial \theta}{\partial S} - P, \tag{4.11}$$

$$m\frac{\partial^2 X}{\partial t^2}\cos(\theta) + m\frac{\partial^2 Y}{\partial t^2}\sin(\theta) = \frac{\partial T}{\partial S} - V\frac{\partial \theta}{\partial S}, \tag{4.12}$$

$$V = -\frac{\partial M}{\partial S}, \tag{4.13}$$

where V is the shear force, M the bending moment, T the tension along the beam, and t the time. The bending moment in the beam is assumed proportional to the local curvature,

$$M = D\frac{\partial \theta}{\partial S}, \tag{4.14}$$

where D is the bending rigidity for a unit width of the beam and assumed to be constant over the length of the beam. Boundary conditions at the clamped and free ends of the beam can be written as

$$X|_{S=0} = 0, \quad Y|_{S=0} = 0, \quad \theta|_{S=0} = 0, \tag{4.15}$$

$$\left.\frac{\partial \theta}{\partial S}\right|_{S=L} = 0, \tag{4.16}$$

$$\left.\frac{\partial^2 \theta}{\partial S^2}\right|_{S=L} = 0. \tag{4.17}$$

Considering that the loading on the beam arises from the pressure difference across the beam,

the tension T is neglected. It is assumed to be small compared to the bending moment and shear force. Therefore, equation 4.12 is superfluous. We integrate equation 4.11 from S to L and making use of the boundary conditions of equation 4.17, we obtain

$$D\frac{\partial^2\theta}{\partial S^2} = -m\sin(\theta)\int_S^L\left(\frac{\partial^2 X}{\partial t^2}\right)d\hat{S} + m\cos(\theta)\int_S^L\left(\frac{\partial^2 Y}{\partial t^2}\hat{S}\right)d\hat{S} - \int_S^L Pd\hat{S}. \tag{4.18}$$

To make the system dimensionless, in accordance with the literature on flag flutter (Eloy *et al.*, 2007; Michelin *et al.*, 2008a), We define the reduced velocity and the mass number, respectively

$$U^* = U_\infty L\sqrt{\frac{m_s}{D}}, \tag{4.19}$$

$$M^* = \frac{\rho_f L}{m_s}, . \tag{4.20}$$

where U_∞ is the free-stream velocity, L is the length of the axial beam or half-length of the normal beam, m_s is the mass per unit length and width of the beam, and ρ_f represents the density of fluid. Dimensionless coordinates, time, and pressure along the beam are as follows,

$$s = \frac{S}{L}, \; x = \frac{X}{L}, \; y = \frac{Y}{L}, \; \tau = \frac{tU_\infty}{L}, \; p = \frac{P}{\frac{1}{2}\rho_f U_\infty^2}. \tag{4.21}$$

By substituting these parameters in equation. 4.18, we can rewrite it in the dimensionless form:

$$\frac{1}{U^{*2}}\frac{\partial^2\theta}{\partial s^2} = -\sin(\theta)\int_s^1\ddot{x}d\hat{s} + \cos(\theta)\int_s^1\ddot{y}d\hat{s} - \frac{1}{2}M^*\int_s^1 pd\hat{s}, \tag{4.22}$$

where $\ddot{x}$ and $\ddot{y}$ represent the second derivative of x and y with respect to τ.

Similarly to Mansfield and Simmonds (1987), we define the deformation potentials:

$$u_b = \int_s^1 xd\hat{s}, \tag{4.23}$$

$$v_b = \int_s^1 yd\hat{s}. \tag{4.24}$$

Upon differentiating these potentials with respect to s twice and using equations 4.10 and 4.21, we get

$$\frac{\partial^2 u_b}{\partial s^2} = -\cos\theta \tag{4.25}$$

$$\frac{\partial^2 v_b}{\partial s^2} = -\sin\theta. \tag{4.26}$$

The deformation potentials of equation 4.23 and equation 4.24 are substituted into equation 4.22 to yield

$$\frac{1}{U^{*2}}\frac{\partial^2\theta}{\partial s^2} = -\ddot{u}_b\sin\theta + \ddot{v}_b\cos\theta - \frac{1}{2}M^*\int_s^1 p\,d\hat{s}. \tag{4.27}$$

The system of equations 4.25–4.27 governs the beam mechanics for three independent variables u, v, θ as a function of time τ and space s. Even when omitting the pressure term, these equations are non-linear. To solve these equations, we adopt the quasi-linearisation approach of Stolte and Benson (1992). Equations 4.25–4.27 are rewritten as

$$\frac{\partial^2 u_b}{\partial s^2} - \theta\sin\tilde{\theta} = -\cos\tilde{\theta} - \tilde{\theta}\sin\tilde{\theta}, \tag{4.28}$$

$$\frac{\partial^2 v_b}{\partial s^2} + \theta\cos\tilde{\theta} = -\sin\tilde{\theta} + \tilde{\theta}\cos\tilde{\theta}, \tag{4.29}$$

$$\frac{1}{U^{*2}}\frac{\partial^2\theta}{\partial s^2} + \theta\left(\ddot{\tilde{u}}_b\cos\tilde{\theta} + \ddot{\tilde{v}}_b\sin\tilde{\theta}\right) = \tilde{\theta}\left(\ddot{\tilde{u}}_b\cos\tilde{\theta} + \ddot{\tilde{v}}_b\sin\tilde{\theta}\right) - \ddot{u}_b\sin\tilde{\theta} + \ddot{v}_b\cos\tilde{\theta} - \frac{1}{2}M^*\int_s^1 p\,d\hat{s}. \tag{4.30}$$

where quantities with the tilde ($\tilde{}$) represent the last known approximation. The tilde quantities were evaluated in the last iteration and the other quantities are to be evaluated. We assume that the differences between the tilde and the non-tilde quantities are small and tend to zero as the scheme converges.

4.2.4   Structure Solver

The structure solver developed in this work solves the discretized equations with a second order central difference method for the spatial terms, and a second order implicit backward Euler method (BDF2) for the time integration. The discretization renders the equations

in the matrix form which are solved using the BiConjugate Gradient STABilized method (BiCGSTAB) to describe the position of the beam in time.

The system of equations 4.28–4.30 are discretized using the finite difference method. We assume N points along the beam, which results in elements with length of $\Delta s = L/(N-1)$. In order to get the discretized from of the system of equations, we substitute the partial derivative terms in space by the following approximate finite differences

$$\frac{\partial^2 u_b}{\partial s^2} = \frac{u_{b_{i+1}}^{n+1} - 2u_{b_i}^{n+1} + u_{b_{i-1}}^{n+1}}{\Delta s^2} + O(\Delta s^2), \tag{4.31}$$

$$\frac{\partial^2 v_b}{\partial s^2} = \frac{v_{b_{i+1}}^{n+1} - 2v_{b_i}^{n+1} + v_{b_{i-1}}^{n+1}}{\Delta s^2} + O(\Delta s^2), \tag{4.32}$$

$$\frac{\partial^2 \theta}{\partial s^2} = \frac{\theta_{i+1}^{n+1} - 2\theta_i^{n+1} + \theta_{i-1}^{n+1}}{\Delta s^2} + O(\Delta s^2), \tag{4.33}$$

and the two time derivatives are substituted by following backward Euler finite differences

$$\ddot{u}_b = \frac{\partial^2 u_b}{\partial \tau^2} = \frac{2u_{b_i}^{n+1} - 5u_{b_i}^{n} + 4u_{b_i}^{n-1} - u_{b_i}^{n-2}}{\Delta \tau^2} + O(\Delta \tau^2), \tag{4.34}$$

$$\ddot{v}_b = \frac{\partial^2 v_b}{\partial \tau^2} = \frac{2v_{b_i}^{n+1} - 5v_{b_i}^{n} + 4v_{b_i}^{n-1} - v_{b_i}^{n-2}}{\Delta \tau^2} + O(\Delta \tau^2). \tag{4.35}$$

After substitution, equations 4.28–4.30 become

$$u_{b_{i+1}}^{n+1} - 2u_{b_i}^{n+1} + u_{b_{i-1}}^{n+1} - \Delta s^2 \theta_i^{n+1} \sin \tilde{\theta}_i^{n+1} = \Delta s^2(-\cos \tilde{\theta}_i^{n+1} - \tilde{\theta}_i^{n+1} \sin \tilde{\theta}_i^{n+1}), \tag{4.36}$$

$$v_{b_{i+1}}^{n+1} - 2v_{b_i}^{n+1} + v_{b_{i-1}}^{n+1} + \Delta s^2 \theta_i^{n+1} \cos \tilde{\theta}_i^{n+1} = \Delta s^2(-\sin \tilde{\theta}_i^{n+1} + \tilde{\theta}_i^{n+1} \cos \tilde{\theta}_i^{n+1}), \tag{4.37}$$

$$\frac{1}{U^{*2}}(\theta_{i+1}^{n+1} - 2\theta_i^{n+1} + \theta_{i-1}^{n+1}) + \Delta s^2 \theta_i^{n+1} \left(\ddot{u}_{b_i}^{n+1} \cos \tilde{\theta}_i^{n+1} + \ddot{v}_{b_i}^{n+1} \sin \tilde{\theta}_i^{n+1} \right)$$

$$+ \frac{\Delta s^2}{\Delta \tau^2}(2u_{b_i}^{n+1} \sin \tilde{\theta}_i^{n+1} - 2v_{b_i}^{n+1} \cos \tilde{\theta}_i^{n+1}) = \Delta s^2 \tilde{\theta}_i^{n+1} \left(\ddot{u}_{b_i}^{n+1} \cos \tilde{\theta}_i^{n+1} + \ddot{v}_{b_i}^{n+1} \sin \tilde{\theta}_i^{n+1} \right)$$

$$+ \frac{\Delta s^2}{\Delta \tau^2} \left[(5u_{b_i}^{n} - 4u_{b_i}^{n-1} + u_{b_i}^{n-2}) \sin \tilde{\theta}_i^{n+1} + (5v_{b_i}^{n} - 4v_{b_i}^{n-1} + v_{b_i}^{n-2}) \cos \tilde{\theta}_i^{n+1} \right] - \Delta s^2 \frac{1}{2} M^* \int_s^1 p \, d\hat{s}. \tag{4.38}$$

The boundary conditions of 4.15 and 4.16 are discretized using second order one-sided finite differences. At the clamped side of the beam we have

$$x\big|_{s=0} = \frac{\partial u_b}{\partial s}\big|_{s=0} = \frac{-1.5u_{b_1}^{n+1} + 2u_{b_2}^{n+1} - 0.5u_{b_3}^{n+1}}{\Delta s} = 0, \tag{4.39}$$

$$y\big|_{s=0} = \frac{\partial v_b}{\partial s}\big|_{s=0} = \frac{-1.5v_{b_1}^{n+1} + 2v_{b_2}^{n+1} - 0.5v_{b_3}^{n+1}}{\Delta s} = 0, \tag{4.40}$$

$$\theta\big|_{s=0} = \theta_1^{n+1} = 0. \tag{4.41}$$

At the free end ($s = 1$) the u_b and v_b are zero based on equations 4.23 and 4.24. In addition, equation 4.16 is the last boundary equation for the free end. Therefore, the discretized boundary equations are

$$u_b\big|_{s=1} = u_{bN} = 0, \tag{4.42}$$

$$v_b\big|_{s=1} = v_{bN} = 0, \tag{4.43}$$

$$\frac{\partial \theta}{\partial s}\bigg|_{s=1} = \frac{0.5\theta_{N-2}^{n+1} - 2\theta_{N-1}^{n+1} + 1.5\theta_N^{n+1}}{\Delta s} = 0. \tag{4.44}$$

The three equations of 4.36–4.38 are linear and can be written in matrix form $AX = B$ to find the solution vector X at each timestep, where X is

$$X = [u_{b1}, \theta_1, v_{b1}, u_{b2}, \theta_2, v_{b2}, ..., u_{bN}, \theta_N, v_{bN}].$$

The approximate solution values are estimated by known solution values of the previous timestep ($\tilde{u}_{b_i}^{n+1} = u_{b_i}^n, \tilde{v}_{b_i}^{n+1} = v_{b_i}^n, \tilde{\theta}_i^{n+1} = \theta_i^n$). Then the linear system of equations of 4.36, 4.37 and 4.38 are solved to find the unknown solution vector. The approximate values are compared to the new solution. If the error is acceptable, then the iterative process is terminated. The difference is calculated using the RMS error given by

$$Error = \sqrt{\frac{1}{N-1}\sum_{i=1}^{N}(X_i^{n+1} - \tilde{X}_i^{n+1})^2}. \tag{4.45}$$

At the first timestep, the solution of the three previous timesteps are needed to solve the linear system of equations and advance in time. The mode shapes of a linear beam is assumed to represent the initial shape of the beam. We consider the shape of the beam at three previous timesteps to be the same as the mode shape of a linear beam ($X^n = X^{n-1} = X^{n-2}$). For a linear beam, the mode shapes can be found analytically using the following equation

$$y = A\left[(\cosh \beta_n x - \cos \beta_n x) + \frac{\cos \beta_n L + \cosh \beta_n L}{\sin \beta_n L + \sinh \beta_n L}(\sin \beta_n L - \sinh \beta_n L)\right], \qquad (4.46)$$

where A is the amplitude of the vibration, L is the length of the beam and β_n values correspond to the natural frequency of the nth mode shape of the beam. The values for the first three mode shapes are shown in table 4.1.

Table 4.1 Values of β_n for the first three mode shapes of a clamped-free beam (from Thomson and Dahleh 1998)

n	$\beta_n L$	w_n/w_1
1	1.8751	1.0000
2	4.6941	6.2669
3	7.8548	17.5475

To determine the stability of the reconfiguring beam, the dimensionless total energy E_b is used, given by

$$E_b = \frac{1}{2}U^{*2}\int_0^1 \left[(\frac{\partial x}{\partial \tau})^2 + (\frac{\partial y}{\partial \tau})^2\right]^2 ds + \frac{1}{2}\int_0^1 (\frac{\partial^2 y}{\partial x^2})^2 ds. \qquad (4.47)$$

where the partial differential terms are approximated by second order finite differences,

$$\frac{\partial x}{\partial \tau} = \frac{1.5x_i^{n+1} - 2x_i^n + 0.5x_i^{n-1}}{\Delta \tau} + O(\Delta \tau^2), \qquad (4.48)$$

$$\frac{\partial y}{\partial \tau} = \frac{1.5y_i^{n+1} - 2y_i^n + 0.5y_i^{n-1}}{\Delta \tau} + O(\Delta \tau^2), \qquad (4.49)$$

$$\frac{\partial^2 y}{\partial x^2} = \frac{\partial \theta}{\partial s} = \frac{0.5\theta_{i+1}^{n+1} - 0.5\theta_{i-1}^{n+1}}{\Delta s} + O(\Delta s^2). \qquad (4.50)$$

4.2.5 Coupling Fluid and Structure Solvers

The decomposition of fluid and the structure domains enforces kinematic and dynamic continuity for the shared interface Γ:

$$\mathbf{V}_\Gamma = \frac{d\mathbf{d}_\Gamma}{dt}, \tag{4.51}$$

$$\boldsymbol{\sigma}_\Gamma^S \cdot \mathbf{n} = \boldsymbol{\sigma}_\Gamma^F \cdot \mathbf{n}, \tag{4.52}$$

where $\mathbf{V}$ is the fluid velocity, $\mathbf{d}$ is the structure displacement, $\mathbf{n}$ is the normal vector at the interface and $\boldsymbol{\sigma}^S$ and $\boldsymbol{\sigma}^F$ are stresses from the structure and the fluid domains, respectively.

In the current project, a nearest neighbor method is implemented for transferring the pressure forces from the fluid to the structure solver. A linear interpolation of the pressure of the two nearest fluid nodes is used as the pressure on the structure nodes. Even though the linear interpolation appears sufficient in our study, we should note that it does not ensure the conservation of energy at each transfer of the pressure and displacement data between two solvers. For the temporal coupling of the flow and structure solvers, both partitioned and iterative partitioned approaches in chapter 2 are implemented.

4.3   Wind Tunnel Experiments

The experiment is performed in the closed-loop wind tunnel (Model 407, ELD. Inc., Lake City, Minnesota) of the Fluid-Structure Interactions Laboratory. The wind tunnel has a test section of 60x60 cm^2 and can produce a maximum air speed of 90 m/s. The operator manually sets the frequency of the wind-tunnel compressor and the corresponding flow velocity is measured by a static Pitot tube placed upstream of the tested specimens.

We adapted the experimental setup from Hassani *et al.* (2016) (figures 4.2–4.3). A 6-axis load cell (ATI GAMMA, ATI Industrial Automation, Apex, North Carolina) measures flow-induced forces on the samples. In the setup, 3 different metallic threaded rods (masts) can be attached to the load cell with adapted acrylic bases machined with a laser encoder (SPEEDY 300, Trotec Laser GmbH, Austria) in the Polytechnique FabLab (PolyFab Nor-

mand Brais). Plates are clamped to the mast using wires wrapped around the rod (figure 4.4).

(a) (b)
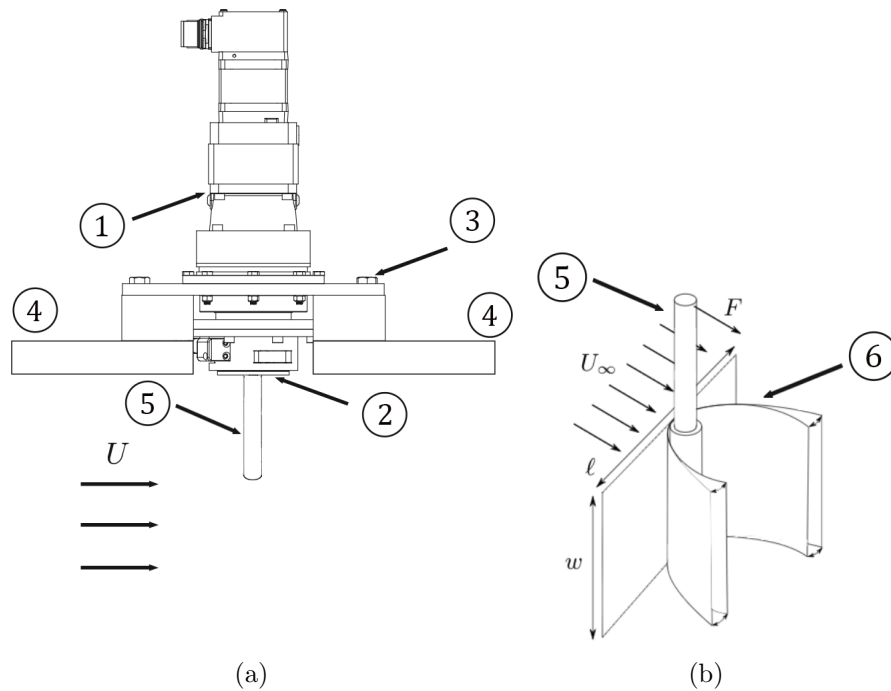
Figure 4.2 (a) side view of the wind tunnel setup. The setup consists of a motor (1), force balance (2), aluminum frame (3), wooden panel (4), metallic mast (5). (b) Isometric view of the mast (5) and the sheet specimen (6).

Figure 4.3 The closed-loop wind tunnel of the Fluid-Structure Interaction laboratory. The test section is shown at the center of the image.
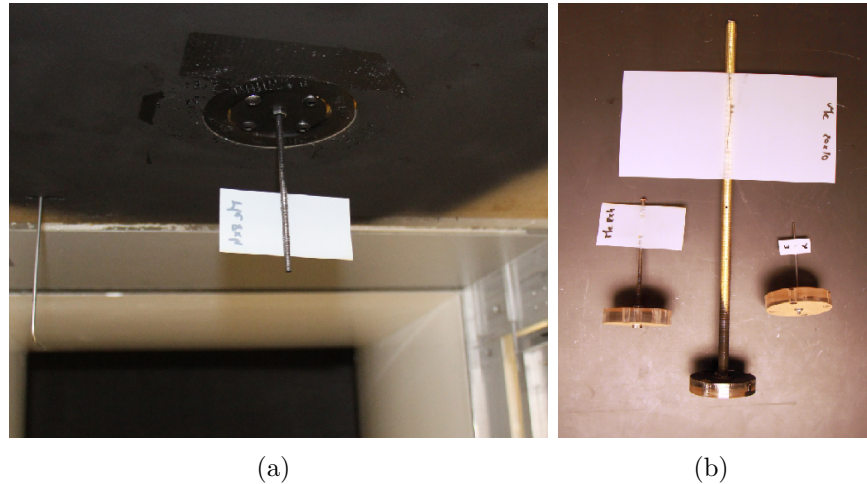
Figure 4.4 (a) The specimen and the mast attached to the top surface of the test section. The Pitot tube is shown in the center-left corner. (b) Three sizes of specimens attached to three different masts (approx. 2, 5 and 10 mm of diameter)

With the aim of diversifying mechanical properties of the tested specimens, and taking account materials accessibility, 5 different materials with specific thicknesses t were selected:

1. Retro-projector acetate (Acetate, $t = 0.1mm$)

2. Polyester (Mylar, $t = 0.09mm$)

3. Polyester (Mylar, $t = 0.184mm$)

4. Polypropylene (Yupo, $t = 0.16mm$)

5. Polytetrafluoroethylene (PTFE, $t = 0.23mm$), particularly chosen for its high density and its theoretically low bending rigidity.

First, the densities per area m_s (kg/m^2) of the sheets are measured by weighting known number of sheets and sizes in an accurate balance. Then, bending properties of the samples are obtained by a flexural 3-point test described in the next section. We cut specimens of different sizes with a laser encoder. Their aspect ratio was all fixed at 2:1 in the experiment to ensure geometrical similarity. Table 4.2 lists detailed information about the flexible rectangular plates tested.

Table 4.2 Characteristics of flexible rectangular plate specimens.

Specimen Label	Length L (m)	Width W (m)	Flexural Rigidity D (Nmm)	Area Density m_s (kg/m^2)
Mylar009	0.024	0.012	0.25	0.112
Mylar009	0.026	0.013	0.25	0.112
Mylar009	0.03	0.015	0.25	0.112
Mylar009	0.04	0.02	0.25	0.112
Mylar009	0.06	0.03	0.25	0.112
Mylar009	0.08	0.04	0.25	0.112
Mylar009	0.1	0.05	0.25	0.112
Mylar009	0.14	0.07	0.25	0.112
Mylar009	0.24	0.12	0.25	0.112
Mylar009	0.27	0.135	0.25	0.112
Acetate01	0.028	0.014	0.43	0.135
Acetate01	0.03	0.015	0.43	0.135
Acetate01	0.04	0.02	0.43	0.135
Acetate01	0.06	0.03	0.43	0.135
Acetate01	0.08	0.04	0.43	0.135
Acetate01	0.1	0.05	0.43	0.135
Acetate01	0.14	0.07	0.43	0.135
Acetate01	0.24	0.12	0.43	0.135
PTFE023	0.036	0.018	0.571	0.41
PTFE023	0.04	0.02	0.571	0.41
PTFE023	0.05	0.025	0.571	0.41
PTFE023	0.06	0.03	0.571	0.41
PTFE023	0.07	0.035	0.571	0.41
PTFE023	0.08	0.04	0.571	0.41
Yupo016	0.04	0.02	1.02	0.151
Yupo016	0.06	0.03	1.02	0.151
Yupo016	0.08	0.04	1.02	0.151
Yupo016	0.1	0.05	1.02	0.151
Yupo016	0.14	0.07	1.02	0.151
Yupo016	0.2	0.1	1.02	0.151
Yupo016	0.24	0.12	1.02	0.151
Yupo016	0.27	0.135	1.02	0.151
Yupo016	0.3	0.15	1.02	0.151
Yupo016	0.4	0.2	1.02	0.151
Mylar0184	0.046	0.023	2.53	0.2476
Mylar0184	0.05	0.025	2.53	0.2476
Mylar0184	0.06	0.03	2.53	0.2476
Mylar0184	0.08	0.04	2.53	0.2476
Mylar0184	0.1	0.05	2.53	0.2476
Mylar0184	0.14	0.07	2.53	0.2476
Mylar0184	0.2	0.1	2.53	0.2476
Mylar0184	0.24	0.12	2.53	0.2476
Mylar0184	0.27	0.135	2.53	0.2476
Mylar0184	0.3	0.15	2.53	0.2476
Mylar0184	0.4	0.2	2.53	0.2476

4.3.1 Flexural rigidity measurement

To measure the flexural rigidity of each material, we use a 3-point flexural test following the ASTM D790 standard procedure. A 5N-capacity load cell (MTS Systems Corp., Eden Prairie, MN) was selected and is fixed on an electromechanical test machine (INSIGHT). The specimen's shape and size were selected according to the standard, i.e. rectangular specimen of 2" (50.8mm) length and 0.5"(12.7mm) width. The specimen are placed on the two inferior noses. Figure 4.5(a) and 4.5(b) show the 3-point test setup and load-deflection curve for one example test, respectively.

<center>(a)   (b)</center>
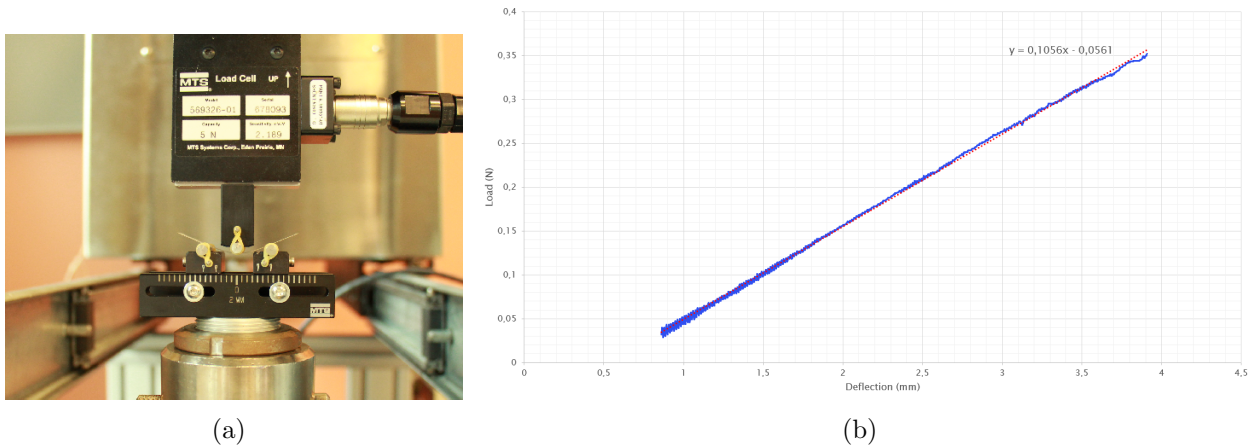
Figure 4.5 Flexural rigidity measurement and sample's bending properties acquisition. (a) 3-point flexural test setup, (b) Slope extraction from load-deflection curve of (Mylar, t = $0.184mm$) sample.

During the downward motion, the cell measures the relation between the deflection in the middle of the sample and the load induced by the specimen bending on the cell. After removing initial motion data (corresponding to non-linear behavior), the tangent modulus of elasticity in bending (E_B) can be extracted from the supposed elastic behaviour (linear range of the load-deflection curve) of the material given by

$$E_B = \frac{s^3 m}{4bt^3},\tag{4.53}$$

where s is the support span (26mm), b is the width of the specimen (12,7mm), t the thickness

of the sample, and m the slope of the tangent to the elastic straight-line portion of the load-deflection curve. Then, the flexural rigidity D is computed by

$$D = \frac{E_B t^3}{12(1 - \nu^2)},\qquad(4.54)$$

where ν is the Poisson's ratio of the material (set to zero for ease of calculation). We have to consider the influence of the plate direction in measuring bending rigidity of the materials, therefore, both length and width bending directions of sheets are tested. Plus, to minimize the error due to previous folding of the sheets, each direction is tested twice, and the value of the bending rigidity is computed from the average of these two measurements.

CHAPTER 5   RESULTS

In the first part of this chapter, we begin with verification of our structural solver where we present a well-known benchmark in the FSI community—a cantilever beam attached to a square cylinder subjected to fluid flow. Secondly, we show the flutter instability of a conventional flag configuration, followed by the reconfiguration of the normal beam with an analysis of its dynamics and post-critical loading. Lastly, we present wind tunnel measurements of the normal beam reconfiguration and flutter.

5.1   Numerical Results

The following parameter values are used for all simulations unless otherwise stated.

$$N = 101, \quad e/L = 0.01, \quad M_\infty = 0.2, \quad tol_f = 10^{-5}, \quad tol_s = 10^{-10}, \tag{5.1}$$

where N is the number of elements along the beam, e/L is the ratio of beam thickness to the length, M_∞ is freestream Mach number, and tol_f and tol_s are stopping criteria for fluid and structure solvers, respectively. The results for the axial beam are derived by a simple partitioned approach, while the results of the normal beam section is obtained by the iterative partitioned approach (Algorithm 2), where tol is set to 10^{-4}.

5.1.1   Structural Solver Verification

In order to verify that the structural solver is correctly implemented, we look at the order of convergence in the space s and time t domains. We test the structural solver by initializing it with a prescribed displacement and simulating the ensuing free vibration. In this case, the first mode shape of the beam described by equation 4.46 is selected as the initial condition.

To find the convergence rate in the time domain, we set the initial value of the timestep $\Delta t = 0.01$ and halve this value seven times, so we simulate the free vibration of the beam

for $\Delta t = 0.01$ to $\Delta t = 0.01 \times 2^{-7}$. The number of elements along the beam N is set to 100. The tip displacement L_2 norm is calculated with respect to that computed for the finest time discretization as the reference to find the error. In the space domain, we also start with 100 elements N and double this value six times to $N = 100 \times 2^6$. At the end of the simulations, the L_2 norm of the position of the beam is calculated with respect to that found with the finest element size Δs as the reference to find the error. The timestep Δt is fixed to 0.01. The error is calculated by

$$Error = \sqrt{\Delta x_i \sum_{i=1}^{n} (Y_{f_i} - Y_i)^2},$$ (5.2)

where Δx is set to the specified Δt or Δs for the time and space domain, and n is the number of beam elements. Figure 5.1 shows the error versus time and space discretization levels. Since the slope of the lines are two and the theoretical order of accuracy in time and space is recovered, we conclude that the code is implemented correctly and is second order accurate in time and space.
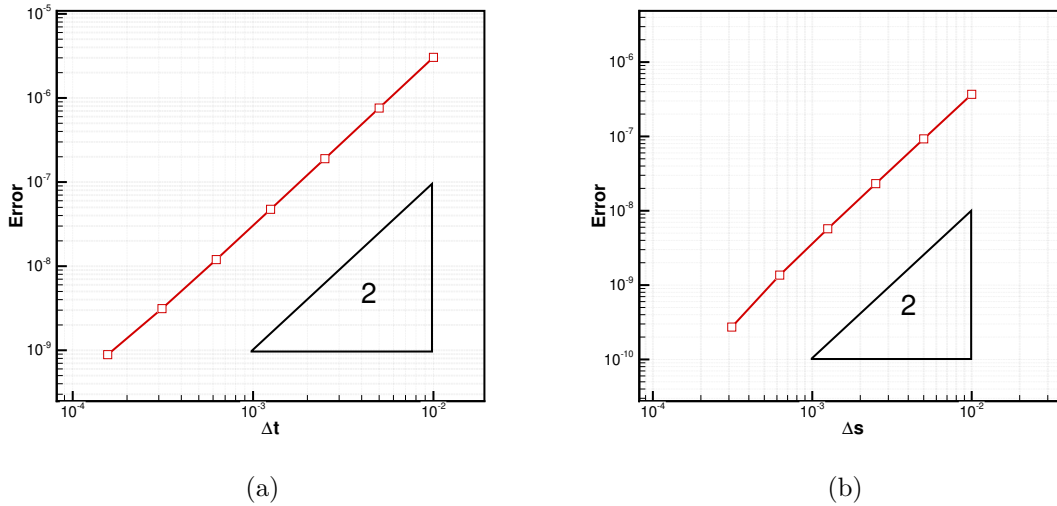

(a)   (b)

Figure 5.1 Verification of the structural solver, order of convergence evaluated (a) in time; and (b) in space. The rate of convergence is 2, since the slope of the lines is 2 in both cases.

5.1.2 A Cantilever Beam Attached to a Square Cylinder

This benchmark was first presented by Wall (1998) and used by many researchers for verification of FSI codes. It consists of a rigid square and a flexible cantilever beam attached to the square (figure 5.2). The physical properties of the fluid and solid domains are shown in table 5.1. The fluid flow properties corresponds to a Reynolds number of 332 with respect to the length of the square. At this Reynolds number, vortices are expected to shed downstream of the square. The cantilever beam is initially positioned horizontally with zero displacement. The vortices interact with the cantilever beam, and the beam undergoes vortex-induced vibrations. The maximum tip displacement in the vertical direction and the frequency of the vibration are used as the verification criteria.

The Mach number is set to $M_\infty = 0.2$ similarly to Sanchez *et al.* (2016). Since the structure solver uses dimensionless numbers, we have to convert the data in table 5.1 to the appropriate dimensionless form. Therefore mass ratio and reduced velocity are set to $M^\star = 0.79$ and $U^\star = 2.37$, respectively. The grid generated by NSGRID is shown in figure 5.3. Two snapshots of the simulation are presented in figure 5.4. As shown in figure 5.5 the beam is initially at rest with zero displacement, and gradually starts to oscillate with the maximum tip displacement of 1.36 cm. The dimensionless frequency of the tip displacements which is evaluated by Fourier analysis is found to be $f = 0.246$, or equivalently 3.15 Hz. These

Table 5.1 Fluid and solid properties used in the Wall (1998) benchmark

Fluid		
density (ρ_f)	1.18×10^{-3}	$kg \cdot m^{-3}$
viscosity (μ_f)	1.82×10^{-4}	$Pa \cdot s$
inlet velocity (U_∞)	51.3	$m \cdot s^{-1}$
Solid		
density (ρ_f)	0.1	$kg \cdot m^{-3}$
Young's modulus (E)	2.5×10^6	Pa
Poisson's ratio (ν)	0.35	-
Beam length (L)	4	m
Beam thickness (e)	0.06	m
Square side length (c)	1	m
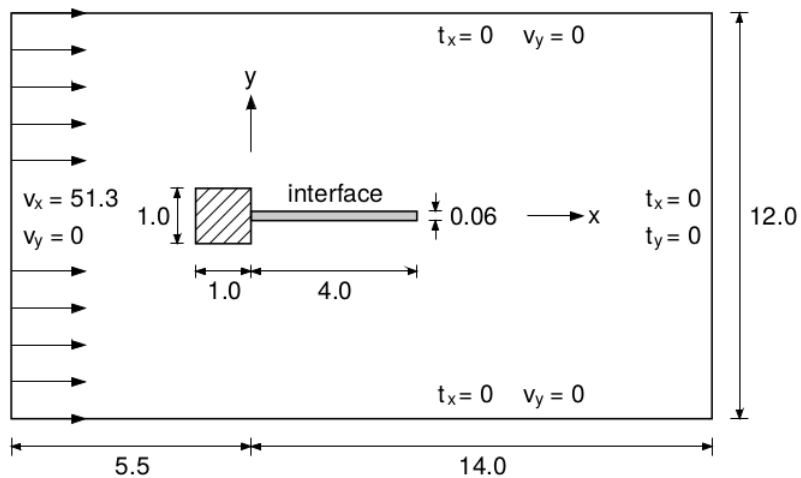
Figure 5.2 Geometry of the Wall (1998) benchmark (Image from Hübner *et al.* 2004)
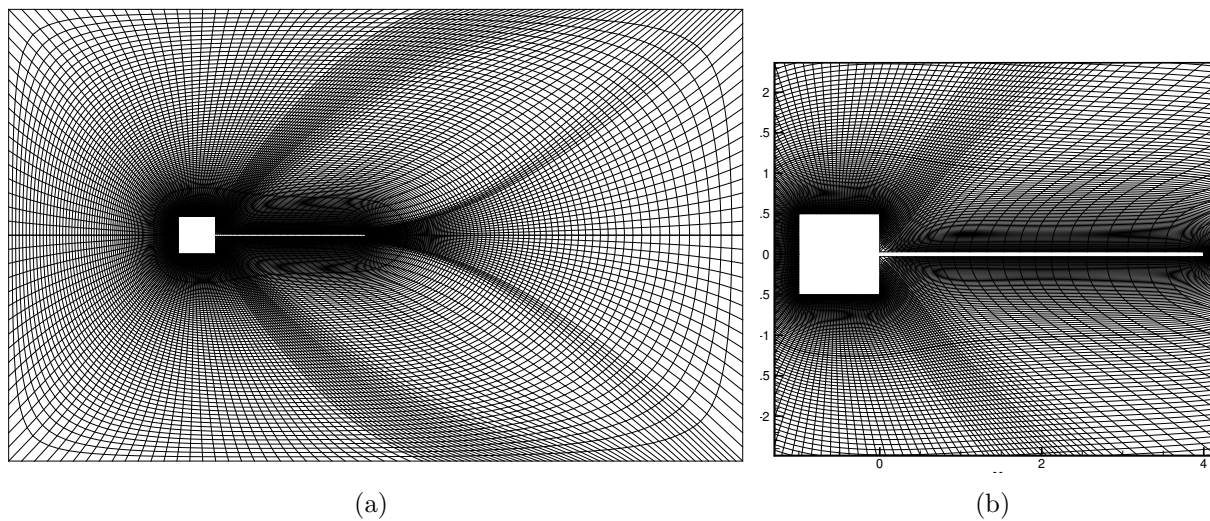
Figure 5.3 (a) The grid generated by NSCODE when the cantilever beam is at rest; (b) simply a close-up of the grid in figure (a).
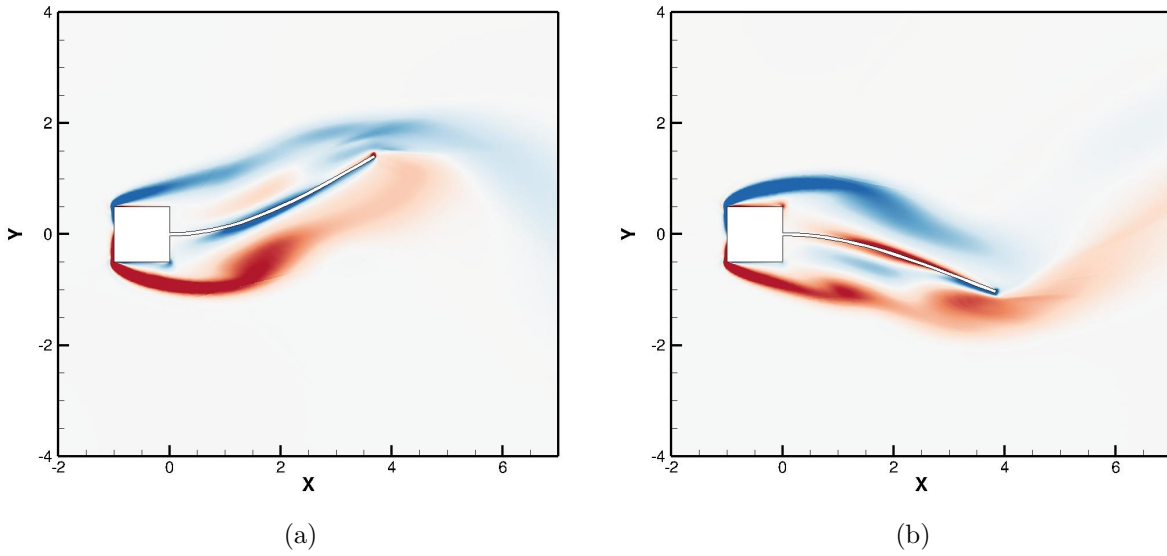
Figure 5.4 Snapshots of the Wall (1998) benchmark in half period of the oscillation from (a) maximum to (b) minimum Ytip displacement. Colors present vorticity magnitude, from -1 (red) to 1 (blue).

result are in very good agreement with the available result in the literature shown in table 5.2.

Table 5.2 Compilation of literature results for the Wall (1998) benchmark.

	Average frequency (Hz)	Max tip displacement (cm)
Wall (1998)	3.08	1.31
Matthies and Steindorf (2003)	2.99	1.34
Dettmer and Perić (2006)	2.96 - 3.31	1.1 - 1.4
Wood *et al.* (2008)	2.78 - 3.125	1.1 - 1.2
Kassiotis *et al.* (2011)	3.17	1.0
Olivier *et al.* (2009)	3.12-3.23	0.8 - 1.0
Present Computations	**3.15**	**1.36**

5.1.3   Stability of Axial Beam Configuration in Fluid Flow

In this section, we consider the stability of axial beam configuration, a classical 2D cantilevered flag with bending rigidity. Figure 5.6 shows the computational domain and a snapshot of the flag deformation in the fluid flow. The clamped end of the beam is located at the center of the circular domain, the radius of which is 50 times the beam length.
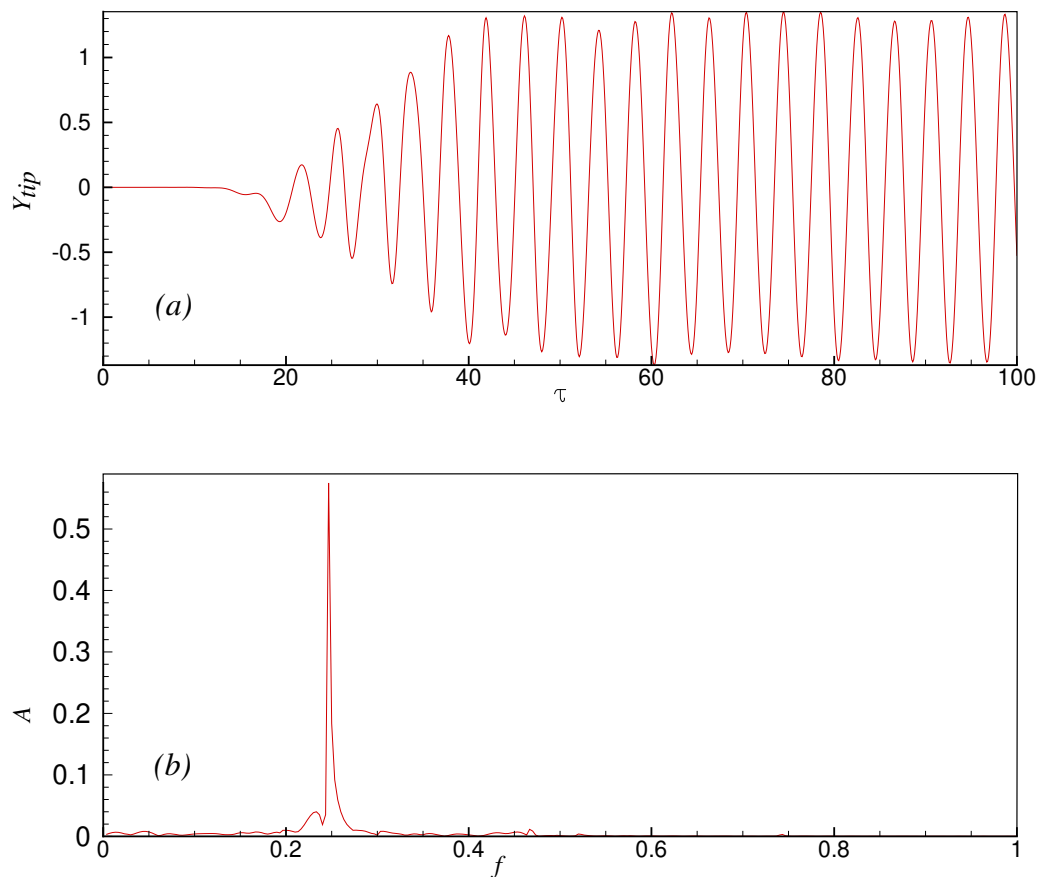
Figure 5.5 Validation simulation of the Wall (1998) benchmark with the parameters of table 5.1: (a) time-trace of the dimensionless tip displacement of the cantilever; (b) its corresponding Fourier transform.

Figure 5.7 shows the timestep convergence study done by estimating the beam total energy with the partitioned approach. As the timestep decreases, the difference in total energy prediction tends to zero, to the extent that the lines correspond to two timesteps of $d\tau = 0.01$ and $d\tau = 0.005$ are almost indistinguishable. In our flag stability study, we set the timestep at 0.01.

To determine the critical velocity at which the flag becomes unstable, the total energy E_b of the flag is monitored. As shown in figure 5.8, for the mass ratio of 0.5, the total energy decreases for the reduced velocity of 7 and 8.4, whereas for the reduced velocity of 9.7 and above the total energy increases with time. Therefore, the critical reduced velocity is between 8.4 and 9.7. Using a bisection method, the critical reduced velocity could be determined with the desired accuracy at each mass ratio.

Figure 5.9(a) maps the performed simulations, marking each one with a circle when the energy decreases and with a cross when the energy increases with time. Tracing a curve to separate the circles and crosses, we can establish the axial beam stability boundary. Three
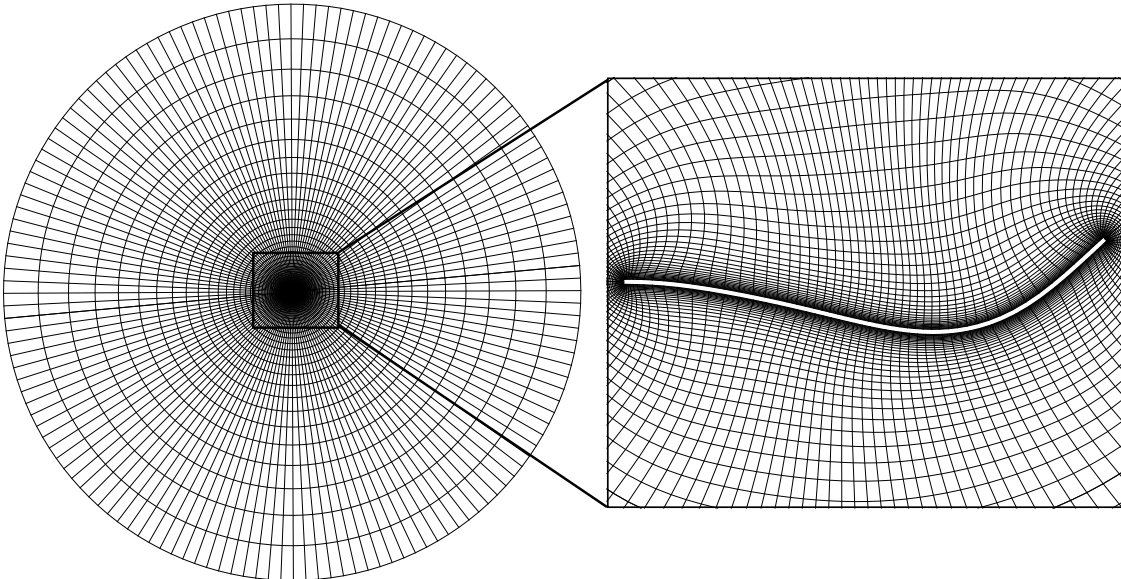
Figure 5.6 Computational domain for the axial beam configuration. A snapshot of the axial beam deformation is shown, where the leading edge is clamped and the rest of the beam can freely move in the flow field.
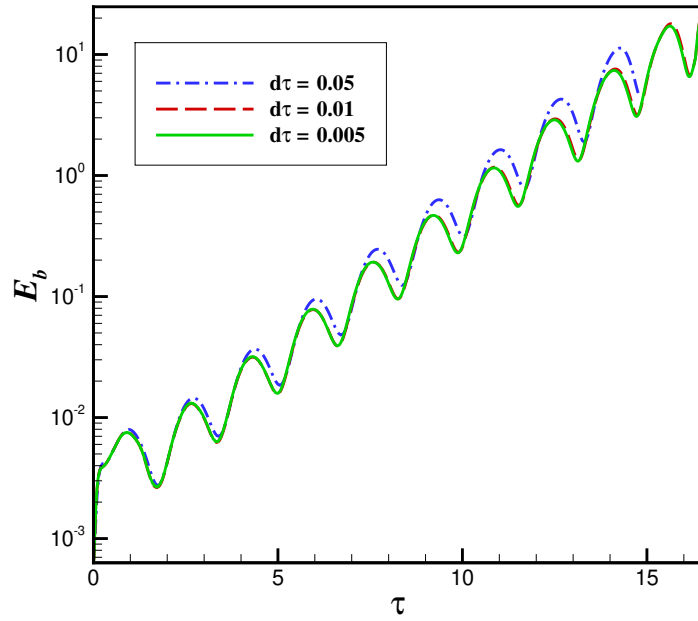
Figure 5.7 Sensitivity of the beam energy computation with the timestep size ($M^\star = 0.5, U^\star = 9$).
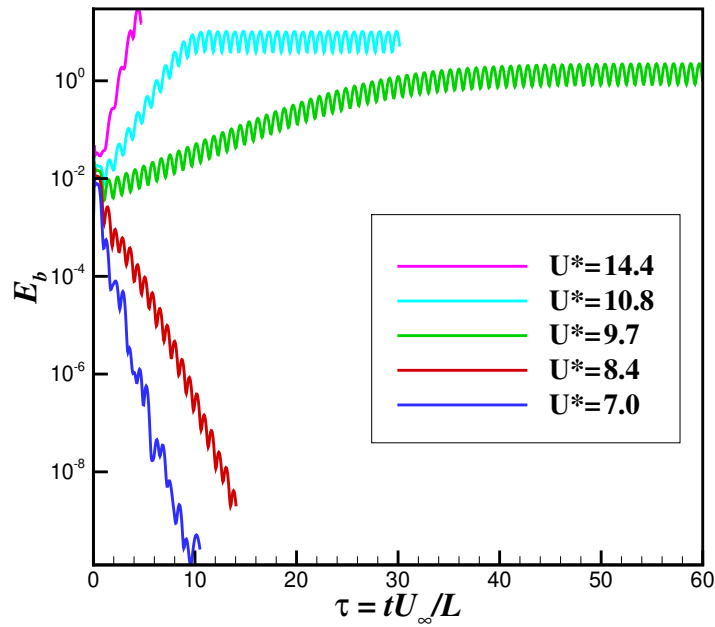
Figure 5.8 Example of the monitored total energy of the beam in our iterative method in finding the stability boundary by varying the reduced velocity ($M^\star = 0.5, U^\star = 9$).

distinct lobes are visible in boundary curve of figure 5.9(a), which correspond to the flutter instability occurring in the second, third and fourth modes of vibration of the beam.

We redraw our computed stability boundary and compare it with those previously obtained for similar systems by Eloy *et al.* (2008) and Michelin *et al.* (2008b) in figure 5.9(b). The agreement between the stability predictions of our model and those in the literature confirms our model's capability to accurately predict the onset of the flutter instability.

Figure 5.10 presents snapshots of the position of the unstable axial beam for three combinations of reduced velocity and mass number, which correspond to the three lobes in figure 5.9(b). At a low mass number of $M^* = 0.5$, the axial beam loses stability in the second beam mode (figure 5.10 a), at $M^* = 3$ it is the third beam mode which becomes unstable (figure 5.10 b), and at $M^* = 10$ the fourth beam dominates the exhibited dynamics (figure 5.10 c). The numerical scheme captures well the limit cycle oscillation of the flag in figures 5.10 (b-c). However, the simple partitioned method diverges for the second mode of vibration (figure 5.10 a) and limit cycle oscillations cannot be simulated. This indicates stronger fluid and structure interaction at lower mass numbers. Hence using a strong coupling approach is essential.

For comparison, the observed dynamics of the fluttering beam simulated with a vortex shedding model by Michelin *et al.* (2008b) is shown for the same parameter values in figures 5.10 (d-f). We can see that for the three cases, there is good agreement with our simulations in terms of mode number and vibration amplitude, although the low mass number case diverges numerically in our simulations.

Normal beam

In this section, we consider the normal beam configuration, which is an idealised system to study the reconfiguration of plants subjected to wind (Gosselin *et al.*, 2010). We use the *chimera*, a.k.a. the *overset*, technique in order to have greater flexibility in grid generation for the normal beam configuration (figure 5.11). The chimera technique allows us to use
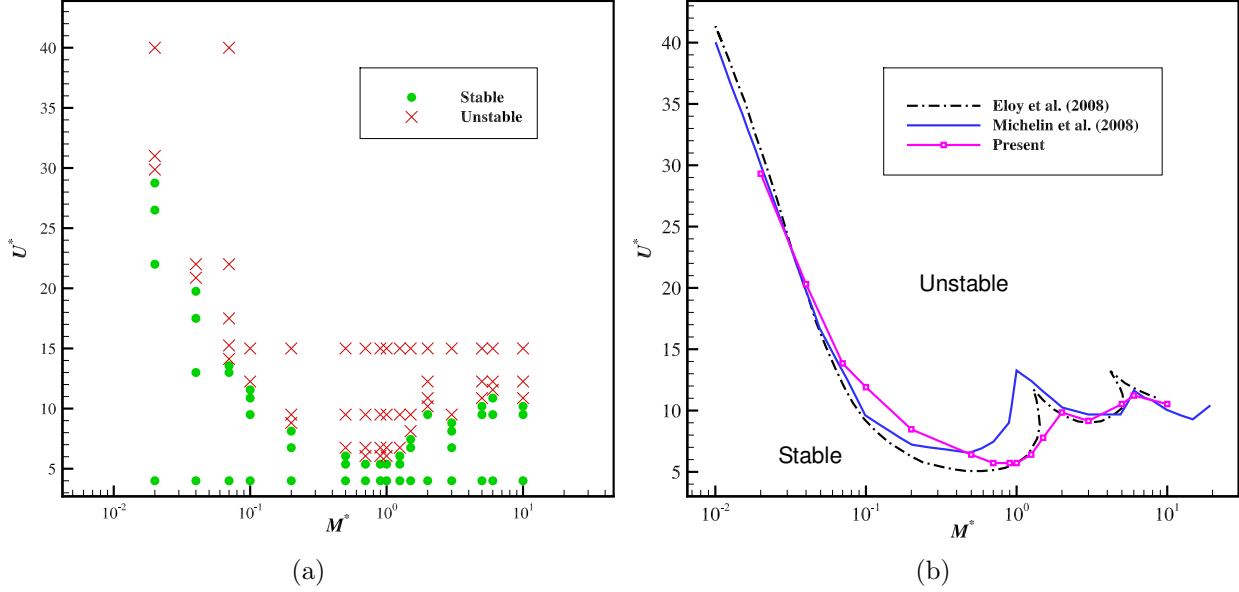
Figure 5.9 Stability map of the axial beam configuration: (a) stable (∘) and unstable (×) dynamics, where each point corresponds to one simulation for a set of mass ratio (M^*) and reduced velocity (U^*); (b) comparison of the critical reduced velocity as obtained with the present numerical procedure with the vortex shedding model of Michelin *et al.* (2008b) and the linear stability analysis of Eloy *et al.* (2008).

two different overlapping grids where the information is exchanged at the grid's boundary via interpolation. The chimera technique was implemented by Guay (2017). We use it to increase the robustness of the developed FSI framework.

The combined NSCODE and beam solver integrates the system in time. To obtain simulations of the normal beam configuration for various reduced velocities, the solver is always initialised with a steady solution of the flow over the rigid normal beam. Then the beam rigidity is gradually decreased with time. This amounts to keeping the Mass $M^\star$ and Mach M_∞ numbers constant, while increasing the reduced velocity $U^\star$, or equivalently the Cauchy number $C_Y = M^\star U^{\star 2}$. A sudden change in reduced velocity may lead to transient effects such as vortex-induced vibrations, which are undesirable for static reconfiguration simulations. To avoid these undesired effects and ensure a gradual variation, the reduced velocity
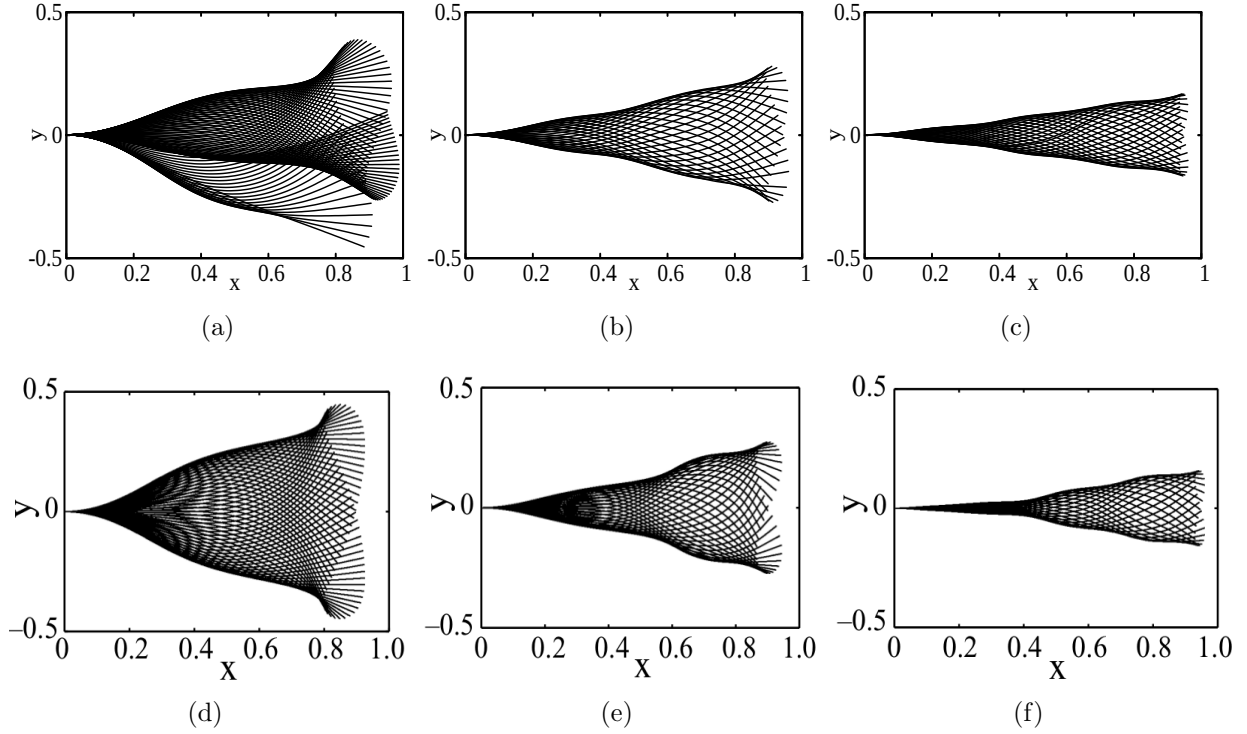
Figure 5.10 Axial beam snapshots as simulated by our model for: (a) $M^* = 0.5, U^* = 9$; (b) $M^* = 3, U^* = 12$; (c) $M^* = 10, U^* = 12$; and by Michelin *et al.* (2008b) with their vortex shedding model for: (d) $M^* = 0.5, U^* = 9$; (e) $M^* = 3, U^* = 12$; (f) $M^* = 10, U^* = 12$.

is ramped-up following a cosine function of simulated time

$$U^* = \frac{1}{2}(U_f^* - U_0^*)\left[1 - cos(\frac{\pi\tau - \pi\tau_i}{\tau_f})\right] + U_0^*, \tag{5.3}$$

where, U_0^* is the initial reduced velocity, U_f^* is the final reduced velocity, τ is the scaled time, and τ_i and τ_f are the initial and the final scaled time by which the bending rigidity is changed to reach its maximum. Beyond τ_f, U^* is maintained constant to study the dynamic response of the system. If the system starts to flutter, then it means that the critical U^* has been reached.

Since we use a time-integration method to investigate the system dynamics, we need to define a criterion to assess the system's stability. The stability criteria is defined in figure 5.12 as an example of an unstable case. After the ramp-up in reduced velocity from $\tau_i = 10$ to $\tau_f = 40$, a constant reduced velocity of $U_f^* = 6$ is reached. We can see that after a transient
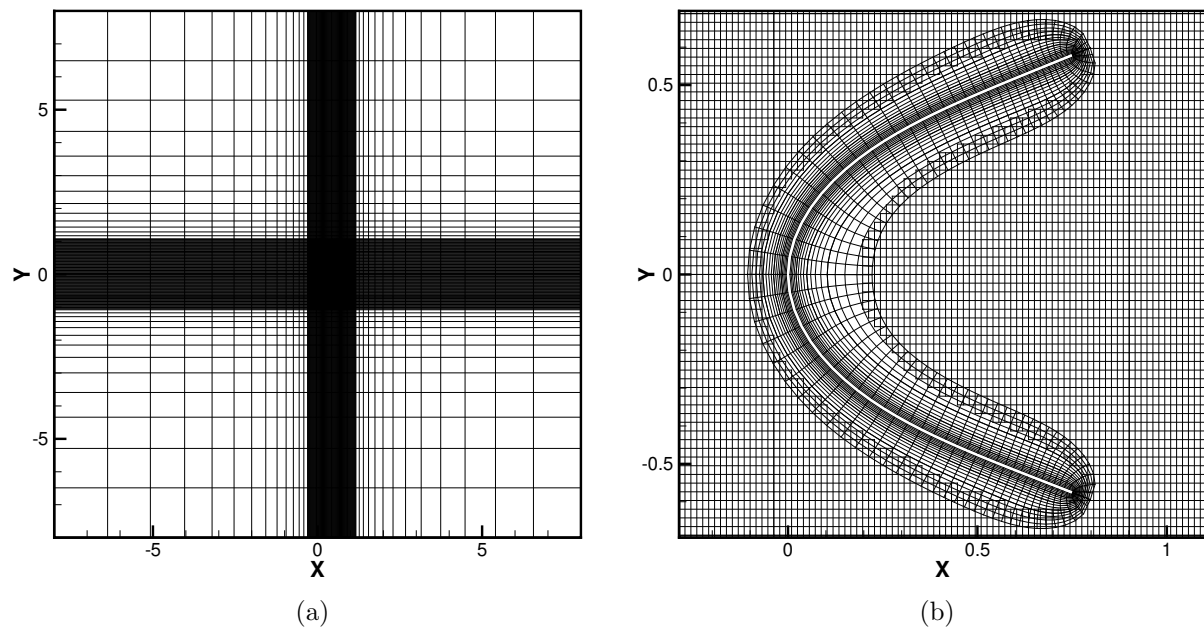
Figure 5.11 Computational domain for the normal beam configuration: (a) the full domain around the underformed beam of length 2; and (b) a close-up of the deformed beam showing the chimera grids, one of them attached to the structure and conforming when the beam is deformed, and a secondary cartesian mesh which is fixed in space. The full domain grid is coarse at four corners, while refined toward the center of the domain where the normal beam is located.

period, the total beam energy reaches a limit cycle oscillation. We set the stability criteria as 10% increase in total energy of the beam E_b compared to the total energy at the end of the ramp-up period E_{bf}. Since in this case the total beam energy increases by more than 10% after $\tau = \tau_f$, we consider this case as an unstable case.

5.1.4   Reconfiguration Limit

Figure 5.13 shows the reconfiguration of a normal beam with mass number $M^* = 0.5$. For a Cauchy number smaller than one—the bending rigidity is large compared to dynamic pressure—the beam is not significantly deformed (figure 5.13 a). As the beam rigidity is decreased, or Cauchy number is increased, the normal beam bends in the flow direction and becomes more streamlined. In addition to streamlining, the projected area reduces. Stream-lining and area reduction are the two basic mechanisms of drag reduction by reconfiguration (Gosselin *et al.*, 2010). For $C_Y < 15.125$ (or equivalently, $U^* < 5.5$), the solver finds a stable stationary solution. Slightly increase of this value leads to flapping due to flutter instability. Figure 5.13 (d) shows several arrangements of the normal beam in one flapping cycle. Further increase in Cauchy number makes the normal beam movement completely irregular.

In order to find the critical velocity for the normal beam case, we run the ramping of the reduced velocity for several integer values of U_f^*, and for a range of mass ratios from 0.1 to 10. Similar to axial beam case, figure 5.14(a) presets the performed simulations, where a circle represents a stable simulation and a cross represents an unstable case. The stability boundary line is chosen as the mean value between the stable and unstable case. shows the obtained critical velocity and compares that to the axial beam case. Figure 5.14(b) present the same stability boundary with respect to Cauchy number. Since the critical Cauchy number increases at higher mass ratios, physically, it indicates that lighter normal beams bend and reconfigure more before flapping. Therefore, reconfiguration is more beneficial at higher mass ratios. For comparison, we draw the stability boundary of both axial nad normal beam configurations in figure 5.15. While the axial beam clearly has 3 lobes corresponding
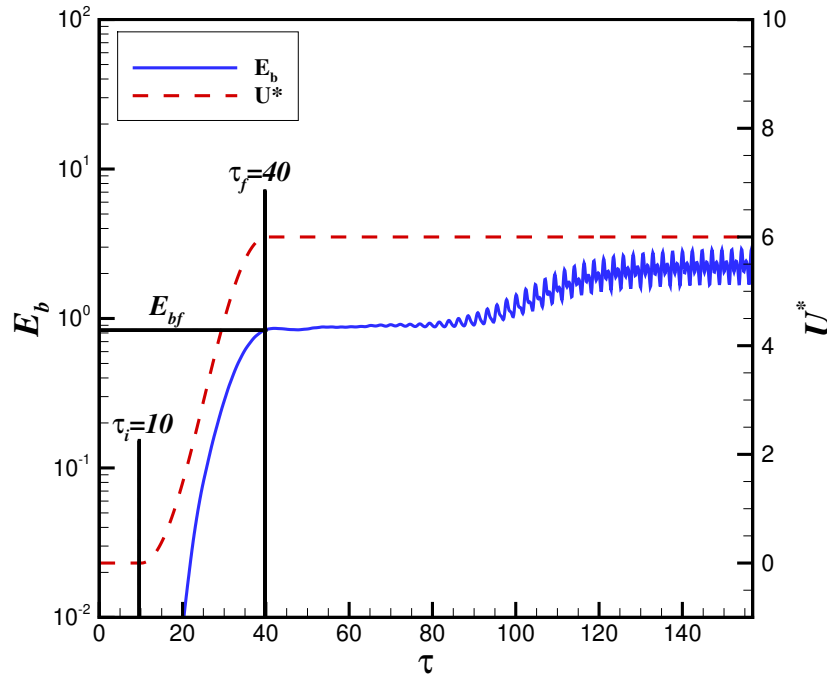
Figure 5.12 Ramping-up of the reduced velocity following a cosine function of time and corresponding simulated total energy of the beam. This is an example of an unstable state ($M^\star = 0.5, U^\star = 6$) for the normal beam.

(a)   (b)   (c)   (d)
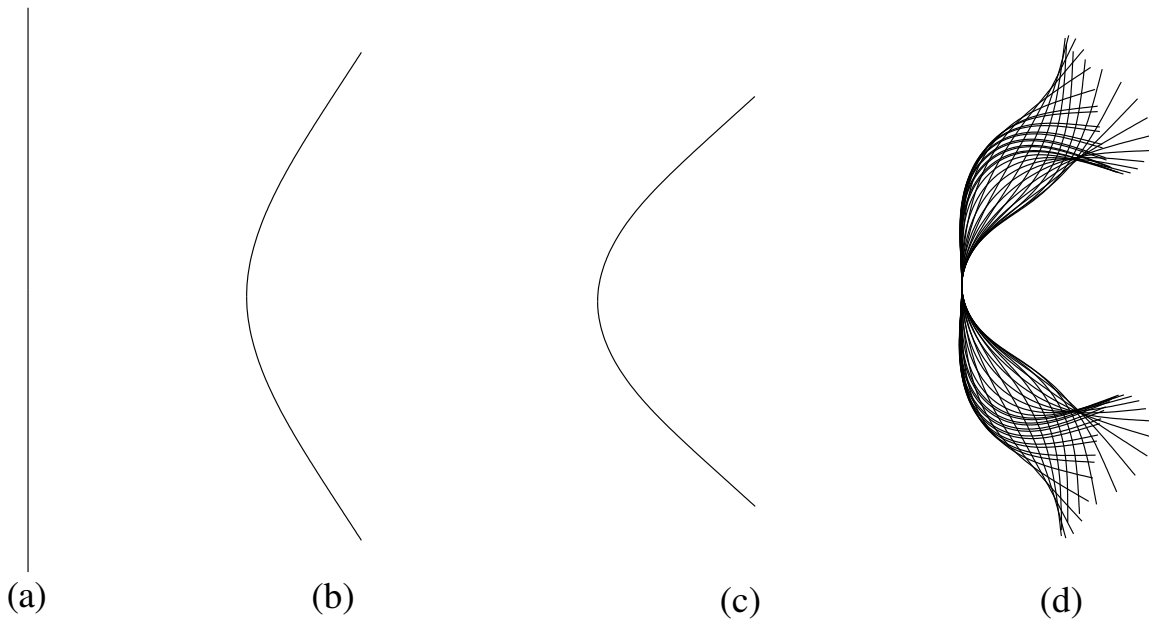
Figure 5.13 Normal beam deformation with increasing Cauchy number. (a) Initial condition of the plate, $C_Y = 0.0005$; (b) $C_Y = 4.5$; (c) $C_Y = 12.5$; and (d) slightly beyond stable point, $C_Y = 21.125$. $M^\star = 0.5$ for all cases. The critical Cauchy number for this mass ratio is 15.125 (or $U^\star = 5.5$).

to transition to different shape modes, the normal beam shows only one lobe. We discuss different normal beam regimes and dynamics in the next section.

5.1.5 Plate Dynamics in Different Mass Ratio Regimes

The different types of plate dynamics observed for the normal beam configuration is broadly classified as the symmetrical and the anti-symmetrical modes. The onset of each regime depends on the mass ratio of the plate, and we observe that the mass ratio governs not only the critical Cauchy number, but also the type of vibration mode in the post-critical regime.

Symmetrical mode

Figure 5.16(a) to 5.16(c) show a symmetrical mode for a plate, where $M^\star = 0.5$. For mass ratios lower than 1.0, we observe that the plate undergoes a constant amplitude limit cycle oscillation for a Cauchy number slightly higher than the critical value. Increasing the Cauchy number leads to a very irregular, chaotic motion of the plate. The figures show that the fluttering plate releases two symmetric vortices from its tips. Since the plate tips are far from each other, the vortices do not interact with one another. Thus, we observe a symmetrical mode.

Anti-symmetrical mode

Figure 5.16(d) to 5.16(f) show an anti-symmetrical mode for a plate, where $M^\star = 5$. For mass ratios equal and greater than 1.0, the plate deformation prior to flutter is relatively large. Thus, the plate tips are close and the shed vortices interact with each other. This leads to an anti-symmetric regime. Similar to the symmetric regime, the plate shows a constant amplitude limit cycle oscillation after reaching the critical Cauchy number and chaotic motion for higher Cauchy numbers.
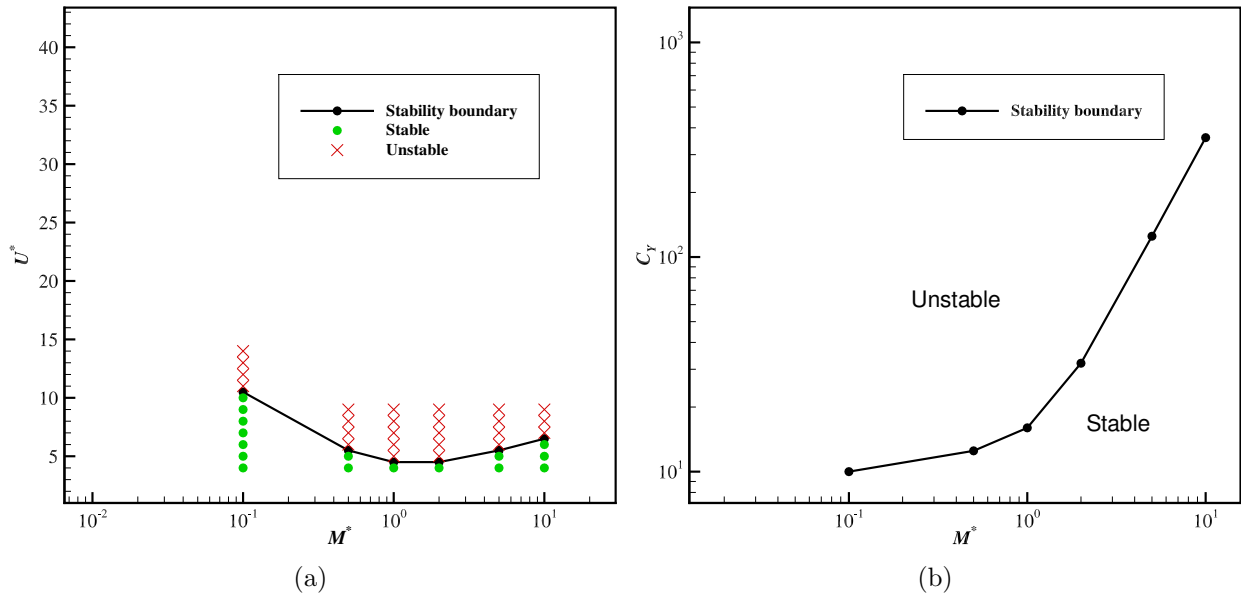
Figure 5.14 (a) Critical reduced velocity for the normal beam configuration obtained with present numerical procedure. Each point correspond to single simulation. (b) critical reduced velocity is transformed to critical Cauchy number and shown as a function of mass ratio.
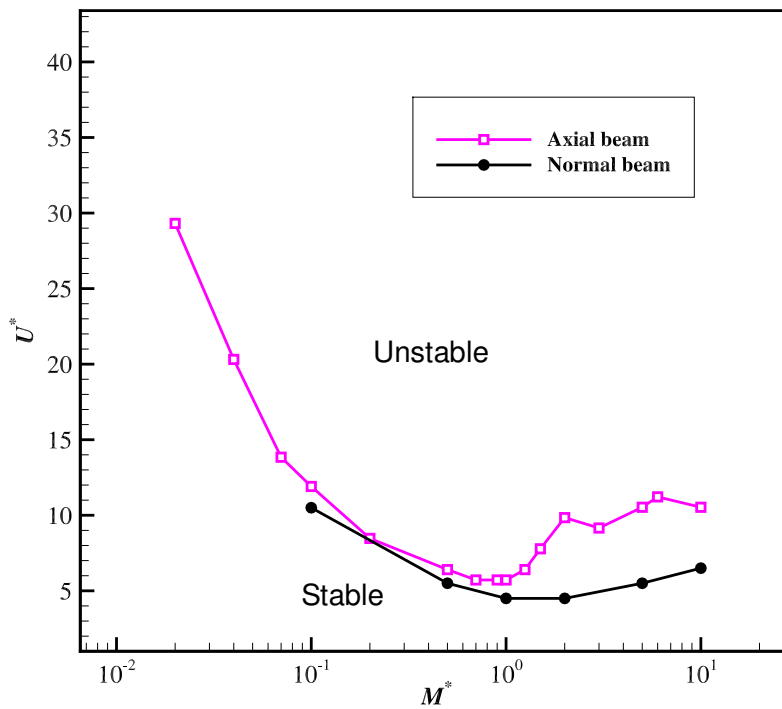
Figure 5.15 The normal beam stability boundary is compared with axial beam case.

(a) $\tau = 0$ (b) $\tau = T/2$ (c) $\tau = T$

(d) $\tau = 0$ (e) $\tau = T/2$ (f) $\tau = T$
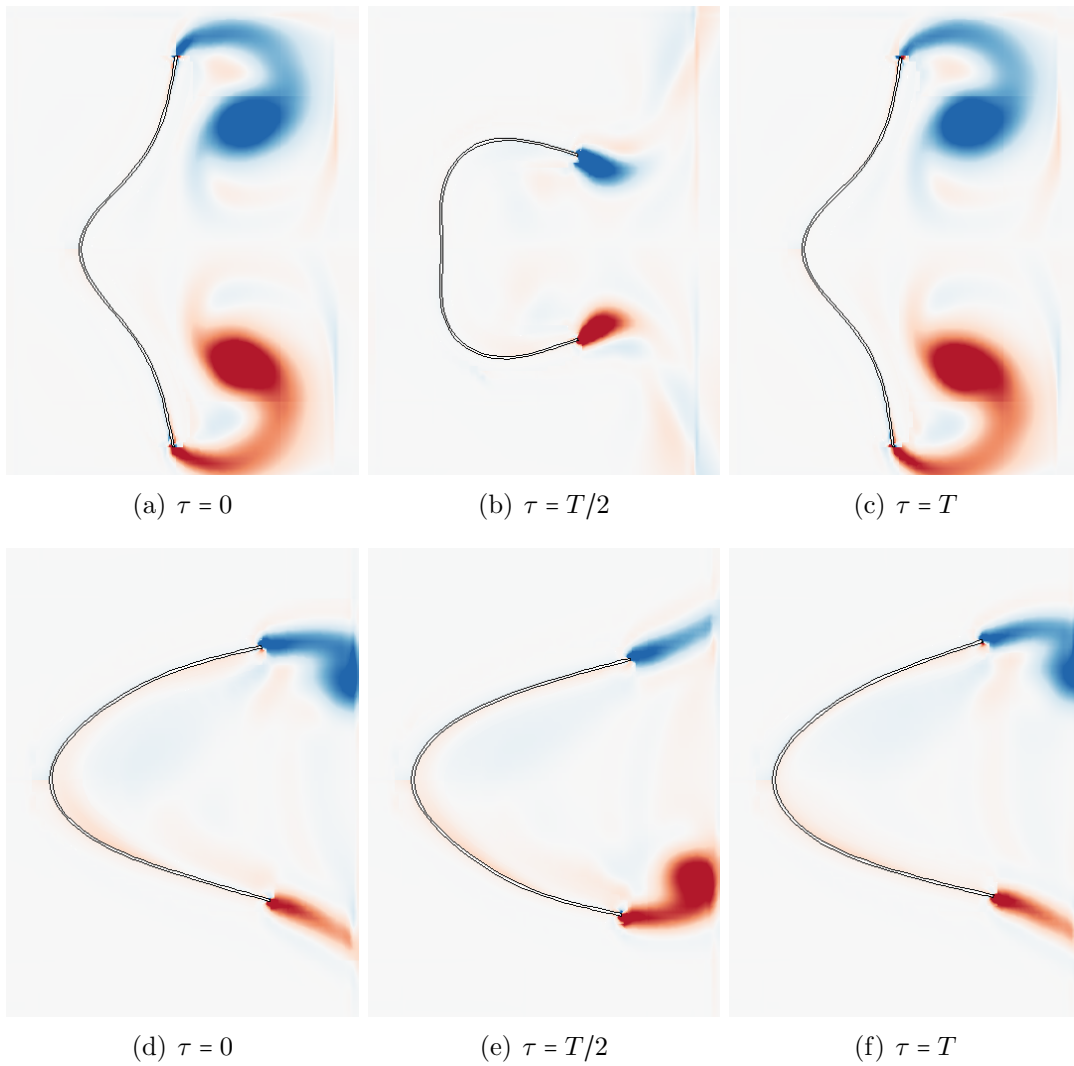
Figure 5.16 (a), (b) and (c) symmetrical mode for $M^* = 0.5$ and $U^* = 6.5$. (d), (e) and (f) anti-symmetrical mode for $M^* = 5.0$ and $U^* = 5.0$. Three snapshots of the normal beam deformation in one period T is shown. Colors present vorticity magnitude, from -3 (red) to 3 (blue).

5.1.6 Spectral Analysis

We look at tip displacement of the upper part of the normal beam in this section to identify the excited modes of the beam, and to see how shedding of vortices change the plate dynamics. To reach this goal, we select two states of the beam, one of which has a mass ratio of less than 1.0 ($M^* = 0.5$), and the other one has a mass ratio greater than 1.0 ($M^* = 2.0$). These two cases are shown in figures 5.17 and 5.18, respectively. Both cases are slightly beyond the stable state.

Figure 5.17 (a) exhibits time-trace of the tip displacement and corresponding Fourier transform. The normal beam is straight in the beginning so Ytip is 1. Then we ramp-up U^* so the normal beam bends and the tip displacement reduces to around 0.7. Thereafter the normal beam begins flapping. Figure 5.17 (b) shows the Fourier transform of the tip displacement, where the first three natural frequency of the beam is added. The three natural frequencies are derived from the axial beam free vibration simulations. From figure 5.17 we can conclude that the dominant excited mode is the second mode of the beam, and the first mode is not excited. This is in agreement with our observation for the axial beam, where the first mode was not unstable. The excitation of the second mode is in some way expected, since at this range of mass ratios, the axial beam is also unstable at its second mode.

Similar procedure is followed to obtain figure 5.18. However, figure 5.18 predicts that when the mass ratios is greater than one, the normal beam dynamics is quite different. In this case, none of the beam modes are excited, but the dominant frequency is equal to the frequency of the vortex shedding behind the plate. which indicates that the plate dynamics is mostly influenced by vortex shedding.

5.1.7 Modulation of Drag due to Reconfiguration and Flutter

To quantify the drag reduction, we use the reconfiguration number $\mathcal{R}$ as the drag of flexible beam D_{flexible} to that of a perfectly stiff one D_{rigid}. Figure 5.19 shows the variation of the reconfiguration number and Cauchy number as a function of the scaled time. We compare

Figure 5.17 (a) Time history of the tip displacement of the normal beam and (b) the frequencies of the tip displacement curve derived by Fourier transform, $M^* = 0.5$, $U^* = 6.5$. The first three natural frequencies of the axial beam are indicated by vertical lines.
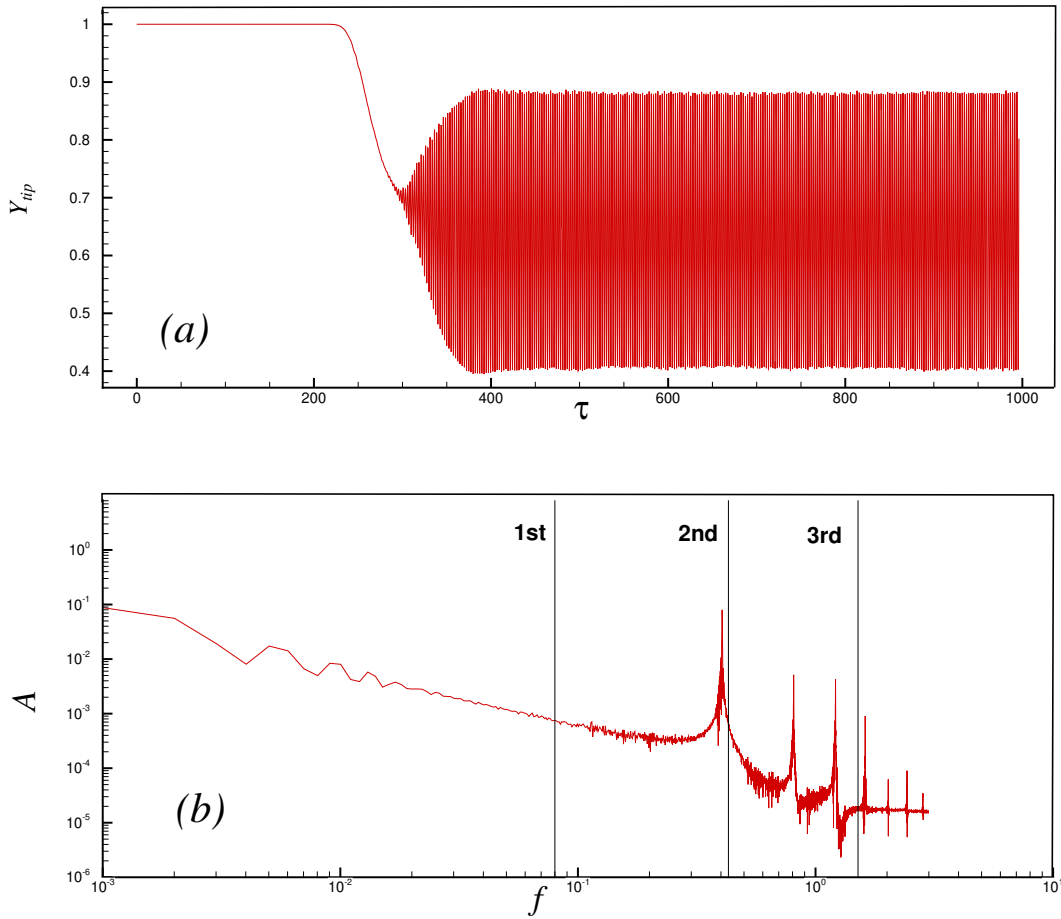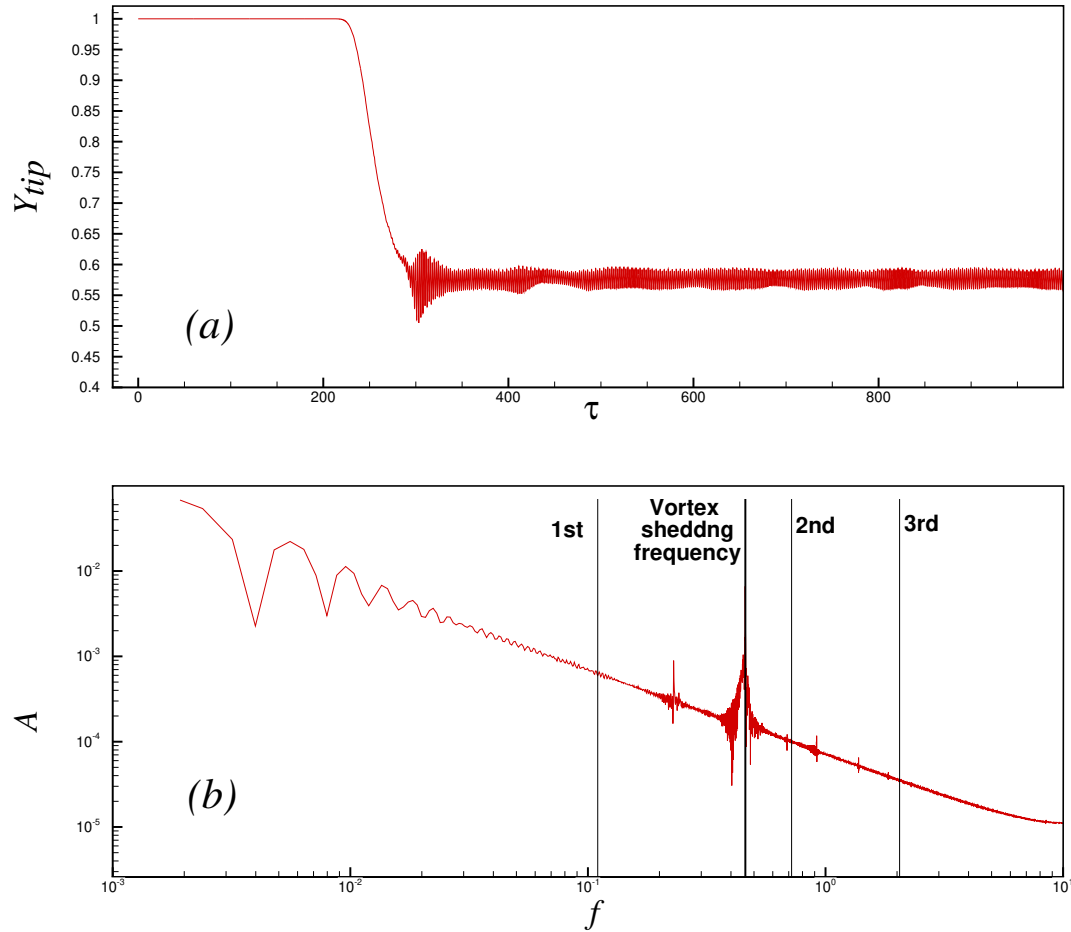
Figure 5.18 (a) Time history of the tip displacement of the normal beam and (b) the frequencies of the tip displacement curve derived by Fourier transform, $M^* = 2$, $U^* = 5$. The frequency of vortex shedding downstream of the normal beam and the first three natural frequencies of the axial beam are indicated by vertical lines.

drag reduction for two cases where $M^* = 0.5$ and $M^* = 1.0$. In both cases the Cauchy number is increased to slightly above the stability limit and not in the the chaotic regime. At low Cauchy numbers, the beam deformation is not significant and its drag is similar to that of an equivalent rigid beam, i.e. $\mathcal{R} \approx 1$. This is shown in figure 5.19(a) and 5.19(b) when $\tau < 200$. For $C_Y \gtrsim 1$, the flow deforms the beam significantly and the reconfiguration number decreases monotonically with increasing Cauchy number. While the reconfiguration number remains below one for $M^* = 1.0$, it becomes greater than one for the case of $M^* = 0.5$. This is in contrast to what Leclercq *et al.* (2018) observed for their normal beam model, where they asserted that we can spot the drag force of a flexible plate to be greater than the rigid plate only in rare "snapping events" in the chaotic regime.

5.2   Experimental Results

We present the experimental data from the wind tunnel tests in this part. We confirm that the oscillations of the normal beam configuration exist in three regimes of symmetrical, anti-symmetrical and chaotic vibrations, similar to the numerical observations. Thomas Raisson from École Polytechnique, France from April 2018 to July 2018 performed the wind tunnel tests under the supervision of Prof. Laurendeau, Prof. Gosselin, and with help from Mohammad Tari in the closed-loop wind tunnel at the Laboratory of Fluid-Structure Interaction in Polytechnique Montreal during his internship.

5.2.1   Normal Beam

To detect the occurrence of flutter, a statistical analysis of drag records is used. For each wind speed U, the drag force F_x is extracted from the record. In addition, the standard deviation of the drag signal normalized by the mean value is computed every 0.2 sec and then averaged during the 30s record to form the coefficient of variation C_v of the drag. A typical observation of the flutter is shown in figure 5.20.

Figure 5.21(a) shows the drag (diamond) and the coefficient of variation C_v (triangles)
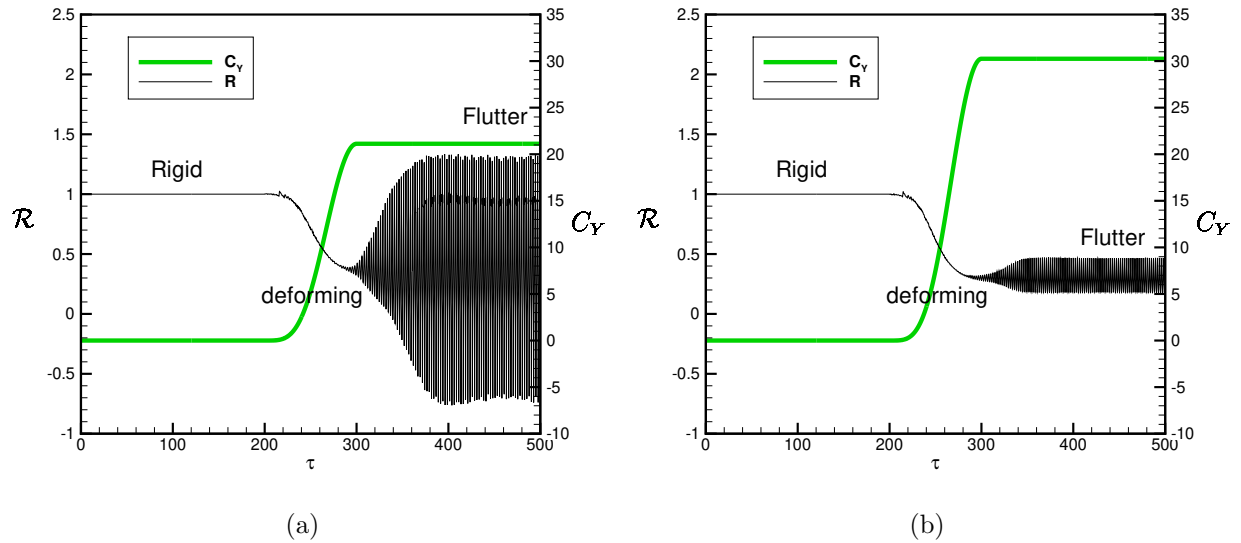
Figure 5.19 Reconfiguration number $\mathcal{R}$ for (a) $M^* = 0.5$ and (b) $M^* = 1.0$. For heavy plates corresponding to $M^* = 0.5$, the loading due to the drag force on fluttering plate increases beyond the rigid plate as reconfiguration number $\mathcal{R}$ increases to greater than one .
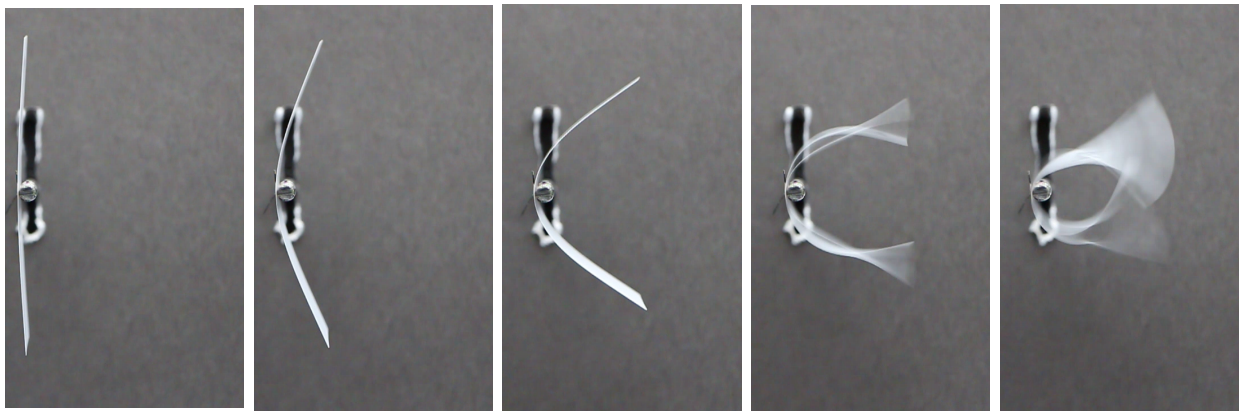
Figure 5.20 Reconfiguration of the normal beam with increasing flow velocity from left to right (Mylar,$t = 0.09mm$, 8cmx4cm). The two pictures on the right show post-flutter state of the normal beam.

during a step by step increase of the flow velocity U. Although the drag curve is not completely smooth, no break is noticeable to indicate where flutter starts. However, a sharp break is observable in C_v curve around a 21 m/s velocity. And this critical velocity matches with visual observation of flutter.

Subsequently, a criteria based on the C_v slope is retained to evaluate between which tested two speeds flutter is occurring:

$$\frac{C_v(U^+) - C_v(U^-)}{U^+ - U^-} \geq 0.05, \tag{5.4}$$

where U^- and U^+ are two subsequent flow velocity of the measurements. The critical velocity is then defined as the lowest velocity at which the condition of equation 5.4 is satisfied. For example, for the specimen plotted in figure 5.21(a), the critical velocity is $U = 20.51$ m/s.

In figure 5.21(b) the critical velocity of the normal beam configuration is shown for all five tested specimens. Experimental results suggest that at lower mass ratios (heavier structures), flutter occurs at higher flow velocities. A more qualitative description is presented in the next section.

At this stage, we can compare the data from the experiments to the output of the simulations to quantify the accuracy of our model. Figure 5.22 shows that the simulation and the experiment predict the similar values, although it seems that the simulation curve underpredicts the instability boundary.

### 5.2.2 Symmetrical, Anti-symmetrical and Chaotic Motion

Once the critical velocity is reached, the plate vibrates which is visible to the naked eye. A camera with 60 f.p.s. frame rate was also used to capture the fluttering motion of the plate. We observe three different modes of vibration: the symmetrical mode where the motions of the both tips were symmetric with respect to horizontal axis, the anti-symmetrical mode where the two sides were in the opposite positions, and the chaotic mode where where the shape of the reconfigured plate was flapping randomly. Depending on the mass ratio M^* of
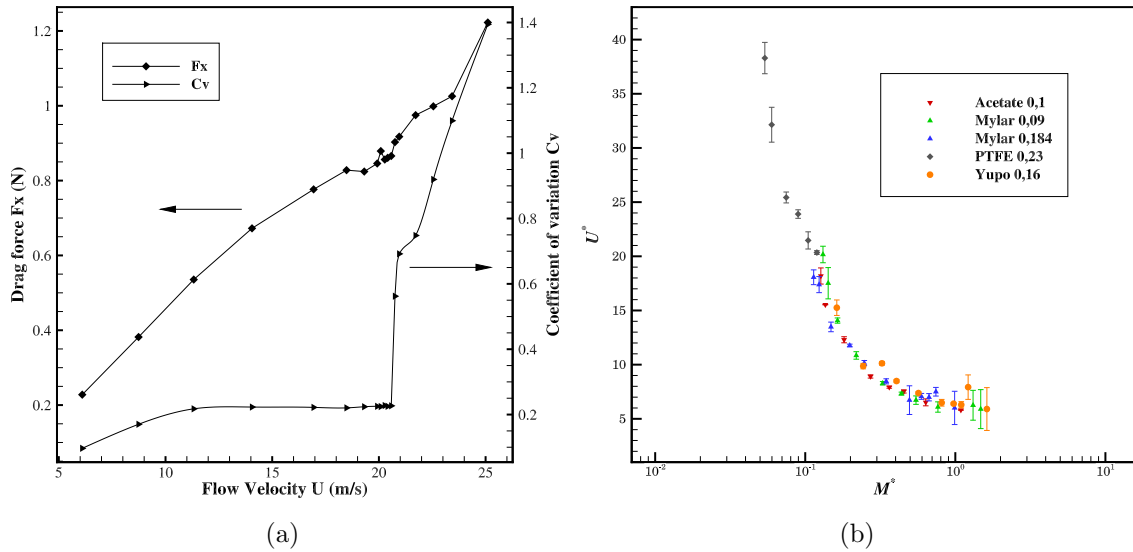
Figure 5.21 (a) The detection of the critical velocity using coefficient of variation of the drag for (Mylar t=0.184mm) specimen. (b) Stability curves of the normal beam configuration. Error bars represent the gap between two subsequent speed measurements providing each critical reduced velocity.
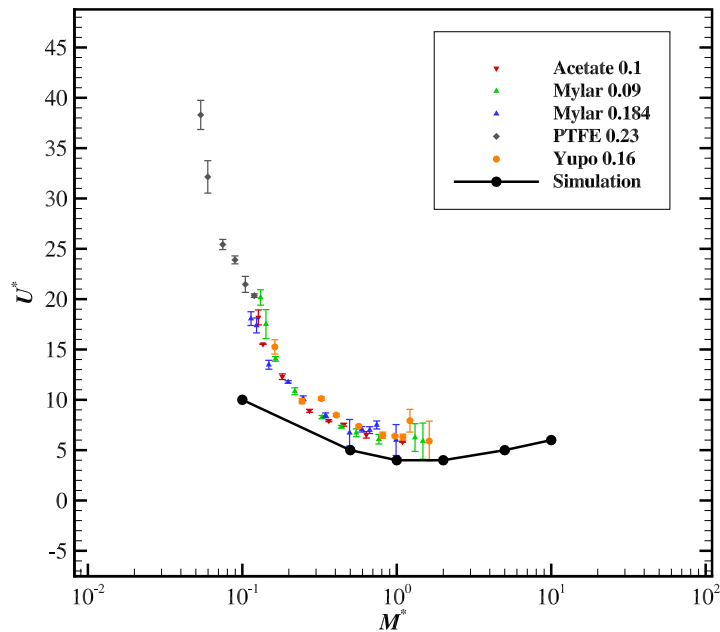
Figure 5.22 The critical reduced velocity of the normal beam configuration in present numerical and experimental setup. Both show the same trend but the experimental result predicts higher reduced velocities. The deviation becomes more apparent in lower mass ratios.

the sheet, three different post critical behaviours was noticed:

1. For higher M^*, corresponding to largest plates, the flutter directly appeared anti-symmetrical.

2. For middle range M^*, the symmetrical mode was observed for low post-critical velocities, and anti-symmetrical is then observed for higher velocities.

3. For lower M^*, the nature of flutter could not be certainly determined, because of the high flutter frequencies relative to the resolution of the camera (60 f.p.s.).

CHAPTER 6   CONCLUSION

6.1   Summary of the Work

In this project an FSI framework is developed using an existing in-house flow solver and a new nonlinear Euler-Bernoulli beam solver. We used the numerical framework to study the interplay of reconfiguration and flutter of a flat plate under the fluid flow. In addition, wind tunnel tests are preformed to validate the output of numerical simulations.

The flow solver NSCODE uses finite volume method to discretize the URANS equation, and it was provided to the author in the beginning of the project. The nonlinear Euler-Bernoulli beam solver is developed in this project, and is second order in time and space. An ALE formulation transfers the motion of the structure to the fluid, while a linear interpolation transfers the fluid pressure values on the surface to the structure solver.

A canonical example of FSI problems, i.e. stability of a convectional flag, is studied to verify the numerical framework. The critical flutter velocity obtained using our method is in agreement with the data in the literature. Later, the same framework is used to analyse reconfiguration of a plate normal to the fluid flow. Numerical and experimental data show that the normal plate reconfigures up to a certain limit before it begins to flutter. The limit of the reconfiguration is described by two dimensionless numbers, Cauchy number and reduced velocity. Similar to the conventional flag problem, this limit depends on mass ratio. An increasing trend between critical flutter Cauchy number and mass ratio is observed, suggesting that reconfiguration is more advantageous for lighter normal beams. Our spectral analysis of the normal beam tip displacement shows that for a mass ratio of less than unity, the plate is excited on its second mode, while for mass ratio of equal and greater than one the nature of the physics is shifted to vortex-induced vibration. Therefore, we observe a symmetrical mode of vibration for the low mass ratios, whereas the plate vibrate in anti-symmetrical mode for higher mass ratios.

6.2 Limitations and Future Works

There are several assumption made in this project that might change the final results. We look at their limitation and propose possible solutions.

In order to decrease the computational cost and complexity caused by turbulence, we used an inviscid flow model to analyze axial and normal beam configurations. Including the viscosity of the fluid would add another dimensionless number to our analysis, i.e. Reynolds number. Although viscous forces are not the input to the structure solver, varying the fluid viscosity can change the flow field variables. The impact of Reynolds number is an interesting path for the future works.

Both simple partitioned and iterative partitioned approach are implemented in this project. We observed that the iterative partitioned approach is more robust as expected. However, numerical experiment shows that for a specific grid and input parameters, the timestep is still limited to a certain value. Additionally, convergence for mass ratios greater than 10 needs more subiterations. Implementing a monolithic FSI solver might fix this issue.

We discovered that the size of the domain for the normal beam case can change the dynamics of the plate. The domain size is fixed at $8L \times 8L$ in simulations, where L is the beam length. Using the domain of $50L$ shows an strong interaction of the shed vortices and the plate, and as soon as $C_y \approx 1$, we observe a coupled vortex-structure dynamics, which unlike the wind tunnel experiments, does not allow us to identify the critical flutter speed. Therefore, all the simulation are presented in the smaller computational domain. We believe strong vortices exist due to two dimensionality of the simulations. The validation of this hypothesis requires comparing the 2D simulation's data with new 3D simulations.

REFERENCES

ABDERRAHMANE, H. A., PAIDOUSSIS, M., FAYED, M. and NG, H. D. (2011). Flapping dynamics of a flexible filament. *Physical Review E*, 84, 066604.

ALBEN, S. (2015). Flag flutter in inviscid channel flow. *Physics of Fluids*, 27, 033603.

ALBEN, S. and SHELLEY, M. J. (2008a). Erratum: Flapping States of a Flag in an Inviscid Fluid: Bistability and the Transition to Chaos [Phys. Rev. Lett. **100** , 074301 (2008)]. *Physical Review Letters*, 101.

ALBEN, S. and SHELLEY, M. J. (2008b). Flapping states of a flag in an inviscid fluid: bistability and the transition to chaos. *Physical review letters*, 100, 074301.

BATHE, K.-J. (2006). *Finite element procedures*. Klaus-Jurgen Bathe.

BLAZEK, J. (2015). *Computational fluid dynamics: principles and applications*. Butterworth-Heinemann.

BLOM, F. J. (1998). A monolithical fluid-structure interaction algorithm applied to the piston problem. *Computer methods in applied mechanics and engineering*, 167, 369–391.

BREUER, M., DE NAYER, G., MÜNSCH, M., GALLINGER, T. and WÜCHNER, R. (2012). Fluid–structure interaction using a partitioned semi-implicit predictor–corrector coupling scheme for the application of large-eddy simulation. *Journal of Fluids and Structures*, 29, 107–130.

CAUSIN, P., GERBEAU, J.-F. and NOBILE, F. (2005). Added-mass effect in the design of partitioned algorithms for fluid–structure problems. *Computer methods in applied mechanics and engineering*, 194, 4506–4527.

COLERA, M. and PÉREZ-SABORID, M. (2018). Numerical investigation of the effects of compressibility on the flutter of a cantilevered plate in an inviscid, subsonic, open flow. *Journal of Sound and Vibration*, <u>423</u>, 442–458.

DE LANGRE, E. (2006). Frequency lock-in is caused by coupled-mode flutter. *Journal of fluids and structures*, <u>22</u>, 783–791.

DE LANGRE, E. (2008). Effects of wind on plants. *Annual Review of Fluid Mechanics*, <u>40</u>, 141–168.

DEGROOTE, J., BRUGGEMAN, P., HAELTERMAN, R. and VIERENDEELS, J. (2008). Stability of a coupling technique for partitioned solvers in fsi applications. *Computers & Structures*, <u>86</u>, 2224–2234.

DETTMER, W. and PERIĆ, D. (2006). A computational framework for fluid–structure interaction: finite element formulation and applications. *Computer Methods in Applied Mechanics and Engineering*, <u>195</u>, 5754–5779.

ELOY, C., KOFMAN, N. and SCHOUVEILER, L. (2012). The origin of hysteresis in the flag instability. *Journal of Fluid Mechanics*, <u>691</u>, 583–593.

ELOY, C., LAGRANGE, R., SOUILLIEZ, C. and SCHOUVEILER, L. (2008). Aeroelastic instability of cantilevered flexible plates in uniform flow. *Journal of Fluid Mechanics*, <u>611</u>, 97–106.

ELOY, C., SOUILLIEZ, C. and SCHOUVEILER, L. (2007). Flutter of a rectangular plate. *Journal of Fluids and Structures*, <u>23</u>, 904–919.

FARHAT, C. and LESOINNE, M. (2000). Two efficient staggered algorithms for the serial and parallel solution of three-dimensional nonlinear transient aeroelastic problems. *Computer methods in applied mechanics and engineering*, <u>182</u>, 499–515.

GOSSELIN, F., DE LANGRE, E. and MACHADO-ALMEIDA, B. A. (2010). Drag reduction of flexible plates by reconfiguration. *Journal of Fluid Mechanics*, 650, 319–341.

GUAY, J. (2017). *Extension of the overset grid preprocessor for surface conforming meshes*. Thèse de doctorat, École Polytechnique de Montréal.

HASANZADEH LASHKAJANI, K., LAURENDEAU, E. and PARASCHIVOIU, I. (2015). Adaptive curvature control grid generation algorithms for complex glaze ice shapes rans simulations. *53rd AIAA Aerospace Sciences Meeting*. 0914.

HASSANI, M., MUREITHI, N. W. and GOSSELIN, F. P. (2016). Large coupled bending and torsional deformation of an elastic rod subjected to fluid flow. *Journal of Fluids and Structures*, 62, 367–383.

HODGES, D. H. and PIERCE, G. A. (2011). *Introduction to structural dynamics and aeroelasticity*, vol. 15. cambridge university press.

HÜBNER, B., WALHORN, E. and DINKLER, D. (2004). A monolithic approach to fluid–structure interaction using space–time finite elements. *Computer methods in applied mechanics and engineering*, 193, 2087–2104.

JOOSTEN, M., DETTMER, W. and PERIĆ, D. (2009). Analysis of the block gauss–seidel solution procedure for a strongly coupled model problem with reference to fluid–structure interaction. *International Journal for Numerical Methods in Engineering*, 78, 757–778.

KASSIOTIS, C., IBRAHIMBEGOVIC, A., NIEKAMP, R. and MATTHIES, H. G. (2011). Nonlinear fluid–structure interaction problem. part i: implicit partitioned algorithm, nonlinear stability proof and validation examples. *Computational Mechanics*, 47, 305–323.

KERBOUA, Y., LAKIS, A., THOMAS, M. and MARCOUILLER, L. (2008). Vibration analysis of rectangular plates coupled with fluid. *Applied Mathematical Modelling*, 32, 2570–2586.

KÜTTLER, U. and WALL, W. A. (2008). Fixed-point fluid–structure interaction solvers with dynamic relaxation. *Computational Mechanics*, <u>43</u>, 61–72.

LECLERCQ, T. and DE LANGRE, E. (2018). Reconfiguration of elastic blades in oscillatory flow. *Journal of Fluid Mechanics*, <u>838</u>, 606–630.

LECLERCQ, T., PEAKE, N. and DE LANGRE, E. (2018). Does flutter prevent drag reduction by reconfiguration? *Proc. R. Soc. A*, <u>474</u>, 20170678.

LEFRANÇOIS, E. and BOUFFLET, J.-P. (2010). An introduction to fluid-structure interaction: application to the piston problem. *SIAM review*, <u>52</u>, 747–767.

LÉVESQUE, A. T. (2015). *Development of an Overset Structured 2D RANS/URANS Navier-Stokes Solver Using an Implicit Space and Non-Linear Frequency Domain Time Operators*. Mémoire de maîtrise, École Polytechnique de Montréal.

MANSFIELD, L. and SIMMONDS, J. (1987). The reverse spaghetti problem: drooping motion of an elastica issuing from a horizontal guide. *ASME J. Appl. Mech*, <u>54</u>, 147–150.

MATTHIES, H. G. and STEINDORF, J. (2003). Partitioned strong coupling algorithms for fluid–structure interaction. *Computers & structures*, <u>81</u>, 805–812.

MICHELIN, S., LLEWELLYN SMITH, S. G. and GLOVER, B. J. (2008a). Vortex shedding model of a flapping flag. *Journal of Fluid Mechanics*, <u>617</u>, 1.

MICHELIN, S., SMITH, S. G. L. and GLOVER, B. J. (2008b). Vortex shedding model of a flapping flag. *Journal of Fluid Mechanics*, <u>617</u>, 1–10.

MICHLER, C., HULSHOFF, S., VAN BRUMMELEN, E. and DE BORST, R. (2004). A monolithic approach to fluid–structure interaction. *Computers & fluids*, <u>33</u>, 839–848.

MILLER, L. A., SANTHANAKRISHNAN, A., JONES, S., HAMLET, C., MERTENS, K. and ZHU, L. (2012). Reconfiguration and the reduction of vortex-induced vibrations in broad leaves. *Journal of Experimental Biology*, <u>215</u>, 2716–2727.

OLIVIER, M., MORISSETTE, J.-F. and DUMAS, G. (2009). A fluid-structure interaction solver for nano-air-vehicle flapping wings. *19th AIAA Computational Fluid Dynamics*. 3676.

PAIDOUSSIS, M. P. (2013). *Fluid-Structure Interactions: Slender Structures and Axial Flow*, vol. 1. Academic Press.

PIPERNO, S. (1994). Staggered time-integration methods for a one-dimensional euler aeroelastic problem. *Raport de Recherche CERMICS*.

PIPERNO, S. and FARHAT, C. (2001). Partitioned procedures for the transient solution of coupled aeroelastic problems–part ii: energy transfer analysis and three-dimensional applications. *Computer methods in applied mechanics and engineering*, 190, 3147–3170.

PIPERNO, S., FARHAT, C. and LARROUTUROU, B. (1995). Partitioned procedures for the transient solution of coupled aroelastic problems part i: Model problem, theory and two-dimensional application. *Computer methods in applied mechanics and engineering*, 124, 79–112.

SANCHEZ, R., PALACIOS, R., ECONOMON, T. D., KLINE, H. L., ALONSO, J. J. and PALACIOS, F. (2016). Towards a fluid-structure interaction solver for problems with large deformations within the open-source su2 suite. *57th AIAA/ASCE/AHS/ASC Structures, Structural Dynamics, and Materials Conference*. 0205.

SANSAS, F. (2016). *Simulation numérique de la dynamique d'une structure élancée flexible dans un écoulement de fluide compressible*. Mémoire de maîtrise, École Polytechnique de Montréal.

SCHOUVEILER, L. and ELOY, C. (2009). Coupled flutter of parallel plates. *Physics of fluids*, 21, 081703.

SI-YING, W., WEN-GANG, D. and XIE-ZHEN, Y. (2013). Transition mode of two parallel flags in uniform flow. *Chinese Physics Letters*, 30, 110502.

STOLTE, J. and BENSON, R. (1992). Dynamic deflection of paper emerging from a channel. *Journal of vibration and acoustics*, <u>114</u>, 187–193.

TANG, L., PAïDOUSSIS, M. P. and JIANG, J. (2009). Cantilevered flexible plates in axial flow: energy transfer and the concept of flutter-mill. *Journal of Sound and Vibration*, <u>326</u>, 263–276.

TAVALLAEINEJAD, M., PAïDOUSSIS, M. P., LEGRAND, M. and KHEIRI, M. (2020). Instability and the post-critical behaviour of two-dimensional inverted flags in axial flow. *Journal of Fluid Mechanics*, <u>890</u>.

THOMSON, W. T. and DAHLEH, M. D. (1998). Theory of vibration with applications.

VAN BRUMMELEN, E. (2009). Added mass effects of compressible and incompressible flows in fluid-structure interaction. *Journal of Applied mechanics*, <u>76</u>, 021206.

VERSTEEG, H. K. and MALALASEKERA, W. (2007). *An introduction to computational fluid dynamics: the finite volume method*. Pearson Education.

VIERENDEELS, J., DEGROOTE, J., ANNEREL, S. and HAELTERMAN, R. (2011). Stability issues in partitioned fsi calculations. *Fluid Structure Interaction II*, Springer. 83–102.

VOGEL, S. (1984). Drag and flexibility in sessile organisms. *American Zoologist*, <u>24</u>, 37–44.

VOGEL, S. (1989). Drag and reconfiguration of broad leaves in high winds. *Journal of Experimental Botany*, <u>40</u>, 941–948.

VON SCHEVEN, M. and RAMM, E. (2011). Strong coupling schemes for interaction of thin-walled structures and incompressible flows. *International Journal for Numerical Methods in Engineering*, <u>87</u>, 214–231.

WALL, W. A. (1998). Fluid-structure interaction based upon a stabilized (ale) finite element method. *Computational Mechanics (World Congress), New Trends and Applications, 1998.*

WOOD, C., GIL, A., HASSAN, O. and BONET, J. (2008). A partitioned coupling approach for dynamic fluid–structure interaction with applications to biological membranes. *International journal for numerical methods in fluids*, <u>57</u>, 555–581.

ZHAO, W., PAiDOUSSIS, M. P., TANG, L., LIU, M. and JIANG, J. (2012). Theoretical and experimental investigations of the dynamics of cantilevered flexible plates subjected to axial flow. *Journal of Sound and Vibration*, <u>331</u>, 575–587.

ZHU, L. (2007). Viscous flow past a flexible fibre tethered at its centre point: vortex shedding. *Journal of Fluid Mechanics*, <u>587</u>, 217–234.